



# Induced synthesis of CeO<sub>2</sub> with abundant crystal boundary for promoting catalytic oxidation of gaseous styrene

Ying Zhang<sup>a,d</sup>, Wenjie Zhu<sup>a,b,\*</sup>, Jichang Lu<sup>a,b</sup>, Wei Liao<sup>a,b</sup>, Ning Qi<sup>e</sup>, Yongming Luo<sup>a,b,c,\*</sup>, Dionysios D. Dionysiou<sup>f</sup>

<sup>a</sup> Faculty of Environmental Science and Engineering, Kunming University of Science and Technology, Kunming 650500, PR China

<sup>b</sup> The Innovation Team for Volatile Organic Compounds Pollutants Control and Resource Utilization of Yunnan Province/The Higher Educational Key Laboratory for Odorous Volatile Organic Compounds Pollutants Control of Yunnan Province, Kunming 650500, PR China

<sup>c</sup> Faculty of Chemical Engineering, Kunming University of Science and Technology, Kunming 650093, PR China

<sup>d</sup> College of Environmental Science and Engineering, Hunan University, Changsha 410082, PR China

<sup>e</sup> College of Physics and Technology, Wuhan University, Wuhan 430072, PR China

<sup>f</sup> Environmental Engineering and Science Program, Department of Chemical and Environmental Engineering (ChEE), University of Cincinnati, Cincinnati, OH 45221-0012, USA

## ARTICLE INFO

### Keywords:

Cerium dioxide  
Gaseous styrene  
Induced synthesis  
Crystal boundary  
Catalytic oxidation

## ABSTRACT

Oxygen vacancies can be used as adsorption-activation sites for reactants, and they can also be used to regulate the electronic structure of catalysts in environmental catalytic oxidation. In the current research on thermal catalytic oxidation, one of the most important issues is the further regulation and design of superior CeO<sub>2</sub> catalysts with abundant oxygen vacancies. Herein, this study reveals a crystallization-inducing strategy to manipulate the exposed morphology, crystal planes, and crystal boundary of CeO<sub>2</sub> catalysts by adding styrene at the synthesis stage. The characterization results demonstrate that the induced activation of styrene can lead to the formation of abundant Ce-Ce crystal boundaries with rich oxygen vacancies in CeO<sub>2</sub>-C<sub>8</sub>H<sub>8</sub> catalysts. Among the synthesized induced CeO<sub>2</sub>-C<sub>8</sub>H<sub>8</sub> catalysts, the short bar-like CeO<sub>2</sub>-C<sub>8</sub>H<sub>8</sub>-130–24 catalyst presented better catalytic activity for styrene oxidation ( $T_{90} = 149\text{ }^{\circ}\text{C}$ ). Moreover, it is found that such a morphological and crystal boundary structure evolution can improve the durability of CeO<sub>2</sub>-C<sub>8</sub>H<sub>8</sub>-130–24. This study provides a novel strategy for modulating the concentration of oxygen vacancies in CeO<sub>2</sub> catalysts.

## 1. Introduction

Due to their role in modulating the physical and chemical properties of metal oxides, increasing attention has been paid to the oxygen vacancies in catalysts, especially in non-homogeneous catalytic reactions. The construction of highly reactive oxygen vacancies is a major area of research in the field of catalytic oxidation. Many studies have shown that oxygen vacancies or clusters of oxygen vacancies are easily formed in the CeO<sub>2</sub> lattice [1,2]. Consequently, cerium-based catalysts have been widely used to reduce the concentration of certain pollutants in automobile exhaust since the 1980 s owing to their excellent redox performance as well as the ability to store and release oxygen [3,4]. Considering the low price and wide application of cerium dioxide and its composites, these materials have become a very important topic in catalytic oxidation research. Various cerium-based catalysts

(incorporating other elements such as Pd, Pt, Ag, Co, and Cu) have been extensively studied [5–8]. Furthermore, a controlled template-free precipitation method was employed to successfully synthesize porous flower-like CeO<sub>2</sub> microspheres [9]. These flower-like CeO<sub>2</sub> microstructures achieved higher low-temperature catalytic activities than conventional CeO<sub>2</sub> nanoparticles. Furthermore, a 3D-ordered mesoporous CeO<sub>2</sub>-based catalyst has been reported to have high stability and strong resistance to deactivation via CO<sub>2</sub>/water vapor during benzene conversion [10]. The synthesis of CeCO<sub>3</sub>OH was induced by the presence of CO gas molecules to obtain a globular protein-like mesoporous structure. After decomposition, spherical mesoporous CeO<sub>2</sub> was obtained, and this structure had better catalytic CO oxidation activity [11,12]. A great deal of research has been conducted to investigate the modification of CeO<sub>2</sub> catalysts using strategies such as ion doping and morphological control. There is no doubt that all these methods ultimately

\* Corresponding authors at: Faculty of Environmental Science and Engineering, Kunming University of Science and Technology, Kunming 650500, PR China.

E-mail addresses: [zhuwenjie17@163.com](mailto:zhuwenjie17@163.com) (W. Zhu), [envirocatalysis@kust.edu.cn](mailto:envirocatalysis@kust.edu.cn) (Y. Luo).

<https://doi.org/10.1016/j.apcatb.2023.123461>

Received 29 June 2023; Received in revised form 28 October 2023; Accepted 1 November 2023

Available online 4 November 2023

0926-3373/© 2023 Elsevier B.V. All rights reserved.

modulate the concentration of oxygen vacancies in CeO<sub>2</sub>. It was reported that the creation of oxygen vacancies on a CeO<sub>2</sub> catalyst surface is beneficial for catalytic oxidation [13–15].

The concentration of oxygen vacancies in CeO<sub>2</sub> can be further regulated by several strategies: (1) in-situ construction, such as the formation of oxygen vacancies during catalyst synthesis; (2) CeO<sub>2</sub> modification (e.g., hetero-atom doping); (3) post-treatment methods (defect engineering strategies such as hydrogen reduction). Currently, many researchers prefer to directly form specific types of oxygen vacancies during the material preparation process [14,16–20]. Explicitly, to develop CeO<sub>2</sub>-based catalysts with high selectivity, activity, and stability by controlling the morphology of CeO<sub>2</sub> during synthesis is very important. Several studies have been conducted by our group on the catalytic oxidation of a volatile organic compound (styrene) by CeO<sub>2</sub> catalysts with different morphologies [13,21]. Simple modifications can be made during the preparation of these CeO<sub>2</sub> catalysts, leading to the modulation of oxygen vacancies and the promotion of the growth of certain crystal surfaces with strong probe substance interactions. Many current researchers are considering whether it is possible to find a new method for preparing CeO<sub>2</sub> catalysts based on existing research foundations. They are also seeking to expose more advantages of crystal facet that have strong interactions with the target and have more oxygen vacancies [14,20,22]. However, this still needs to be further explored.

A significant amount of research on the interface engineering of CeO<sub>2</sub> has been performed to design new CeO<sub>2</sub> catalysts with abundant oxygen vacancies and improved catalytic performance. CuO-CeO<sub>2</sub> catalysts were prepared by a hydrothermal process, and the Cu-Ce interface caused changes in the intermediates formed during the catalytic oxidation of toluene [3]. The Pt-O-Ce interface formed in a Pt<sub>1</sub>-CeO<sub>2</sub> catalyst has higher degree of distortion, preventing thermal instability through strong metal-support interactions [23]. The above work demonstrates that ongoing research is focused on studying the effects of doping on the interfacial interactions between two metals. However, bimetallic interfaces are limited in their practical application due to the aggregation of loaded or doped metals caused by synthesis conditions or high reaction temperatures. This aggregation leads to a decline in catalytic degradation performance. Actually, crystal interfaces do not only exist in bimetallic materials. It is well known that mesocrystals are a class of materials with nanoparticle superstructures formed by the self-assembly of nanocrystals in a crystallographically ordered manner, and these materials possess crystal interface structures [4,24]. The excellent properties of mesocrystals have been extensively studied for photocatalytic applications. The grain boundaries in mesocrystals, as planar defects, can directly and effectively modulate the surface atomic and electronic structure [25]. This significantly alters the intrinsic reactivity of nanocrystalline materials. Using a surfactant (Pluronic P104), Li et al. [26] synthesized a CeO<sub>2</sub> catalyst with homogeneous Ce-Ce interfaces through a self-flaming method. This catalyst demonstrated excellent catalytic combustion performance for toluene. However, how else can Ce-Ce homogeneous interfaces be formed in CeO<sub>2</sub> catalysts? What other methods are available to introduce cluster-type oxygen vacancies (not just single oxygen vacancies) in CeO<sub>2</sub>? “Waste to waste” is a goal that has been pursued by researchers in recent years. However, using the spear of pollutants to attack the shield of pollutants has been a concern of some scholars [27]. These researchers have reported that ultra-high molecular weight fluorinated nanoparticles have highly selective adsorption properties for small fluorinated molecules [27,28]. This leads us to wonder whether the introduction of contaminants can have an induced modification effect during material synthesis: for example, by increasing the adsorption capacity for the pollutant or by microscopically changing the morphology of the material and selectively exposing crystalline facets.

Volatile organic compounds (VOCs) are a significant category of air pollution source. VOCs are generally harmful to human health, and some VOCs are carcinogenic [29]. Styrene is a typical VOC with a strong oak odor that has many applications in the rubber, paint manufacturing,

and plastic industries [30]. The degradation of styrene vapor in air has been investigated in some studies [31–33]. Nevertheless, the thermocatalytic oxidation of styrene is not very well-studied in the field of VOC catalysis. The primary challenge in the catalytic oxidation of styrene is developing a robust catalyst with abundant oxygen vacancies while optimizing catalyst durability. Only a few studies have explored the catalytic oxidation of styrene using novel induced CeO<sub>2</sub> catalysts. Therefore, this work proposes using styrene as a probe molecule introduced into the CeO<sub>2</sub> preparation process to achieve the efficient catalytic degradation of styrene.

Based on the existing research of our group and the extensive studies of using CeO<sub>2</sub> for VOCs (styrene) catalytic oxidation, this study explores the microstructure and regulation of cerium dioxide, and investigates the catalytic oxidation performance of styrene in the prepared induced CeO<sub>2</sub> catalysts. Liquid styrene, as an organic solvent (inducer), is added during the CeO<sub>2</sub> catalyst preparation process, guided by the idea of “using the spear of styrene to attack the shield of styrene”. Due to the induction effect of styrene, the growth of crystal planes (CeO<sub>2</sub>-111) that strongly interact with styrene and the evolution of the CeO<sub>2</sub> morphology are promoted, leading to the formation of homogeneous Ce-Ce interfaces, and improving styrene adsorption and catalytic conversion. Distinct grain boundaries are formed due to the induced crystallization of styrene, resulting in more oxygen defects. The induced CeO<sub>2</sub>-C<sub>8</sub>H<sub>8</sub>-130–24 catalyst (prepared at 130 °C for 24 h) exhibits the best performance for the catalytic oxidation of styrene. This research provides helpful guidance for the degradation of styrene in air and for the synthesis of CeO<sub>2</sub> catalysts to remove gas pollutants in the future.

## 2. Experimental

### 2.1. Materials and catalyst preparation

All reagents in the experiments were used without further purification. The CeO<sub>2</sub>-C<sub>8</sub>H<sub>8</sub> (induced) catalysts were synthesized by solvothermal method. First, 6.0 g Ce(NO<sub>3</sub>)<sub>3</sub>·6 H<sub>2</sub>O (99.0%) was dissolved in 6 mL deionized water. Then, liquid-styrene (>99.5%) with a mass fraction of 0.5% was added to 156 mL glycol (98%), and this mixture was stirred for 15 min. Next, 2 mL of glacial acetic acid (99.5%) was added to the styrene solution. Finally, both solutions were mixed and stirred for 30 min. This mixed solution was poured into a microreactor and heated at 130 °C (140 °C, 120 °C, 110 °C) for 24 h (48 h, 36 h, 18 h, 12 h, 6 h). After the samples were obtained, they underwent multiple washings with alcohol and deionized water, followed by drying in an oven at 60 °C overnight and subsequent calcination at 500 °C for 2 h in a muffle furnace. For comparison, a CeO<sub>2</sub>-NoC<sub>8</sub>H<sub>8</sub> (non-induced) catalyst was also prepared using a microreactor without the addition of liquid styrene. The specific process for the preparation of these induced CeO<sub>2</sub> catalysts is shown in Fig. 1. To provide a comparison, liquid-phase styrene is replaced by other surfactants. The difference between the preparation methods of CeO<sub>2</sub>-CTAB-130–24 and CeO<sub>2</sub>-SDS-130–24 compared to CeO<sub>2</sub>-C<sub>8</sub>H<sub>8</sub>-130–24 is that the added liquid-phase styrene has been replaced with cetyltrimethylammonium bromide (CTAB) and dodecyl sodium sulfate (SDS).

### 2.2. Catalytic activity tests

Catalytic performance of the synthesized catalysts was tested in a self-built reactor. The sample (200 or 100 mg, 40–60 mesh) was stabilized by quartz cotton and placed in the middle of a quartz tube. The inlet stream was 600 ppm/100 ppm styrene with 25% Air, the total gas flow rate was 50 mL/min (weight hour space velocity (WHSV) = 15,000 mL/(g·h) or 30,000 mL/(g·h)). The concentration of styrene and CO<sub>2</sub> in outlet gas were continuously detected by Gas chromatography with two flame ionization detectors and methane conversion furnaces (GC-FID, GC9790Plus, Fuli). One of the FID detectors with a methane conversion furnace can convert CO/CO<sub>2</sub> into CH<sub>4</sub>. These tests

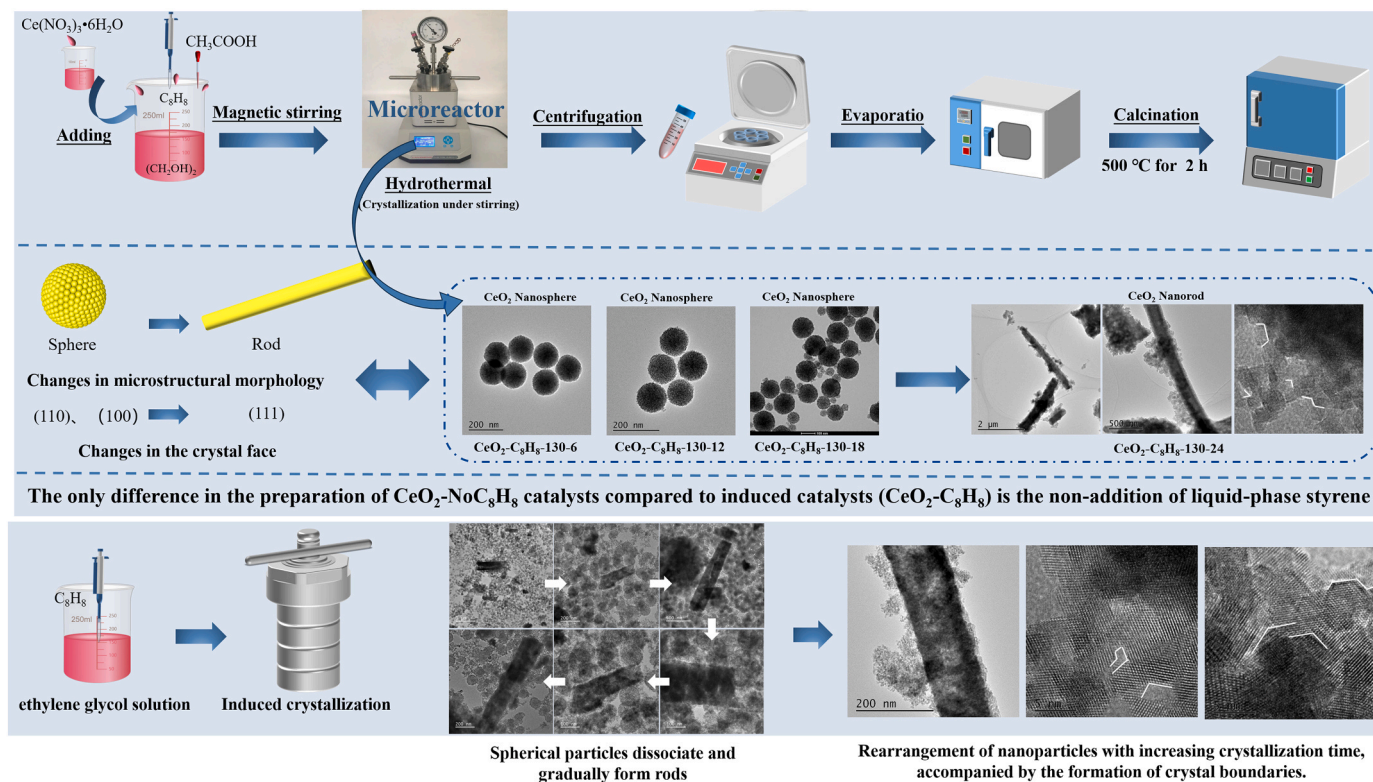


Fig. 1. The process for the preparation of induced  $\text{CeO}_2$  catalysts.

were performed in the temperature from  $30^\circ$  to  $350^\circ\text{C}$  (with a temperature interval  $25^\circ\text{C}$ ). Styrene conversion is defined as follows:

$$\text{Styrene conversion}_T = \frac{\text{Styrene}_0 - \text{Styrene}_T}{\text{Styrene}_0} \quad (1)$$

where  $\text{Styrene}_0$  is the inlet concentration of styrene, and  $\text{Styrene}_T$  is the outlet concentration of styrene at reaction temperature ( $T$ ).

The  $\text{CO}_2$  yield was calculated by Eq. (2):

$$\text{CO}_2 \text{ yield } (\%) = \frac{C_{\text{CO}_2\text{outlet}} - C_{\text{CO}_2\text{inlet}}}{8 \times C_{\text{styrene inlet}}} \times 100\% \quad (2)$$

The reaction rates and normalized reaction rates by surface area were calculated by Eqs. (3) and (4), respectively:

$$r_{(\text{styrene})} = \frac{C_{\text{styrene}} \times X_{\text{styrene}} \times F}{m_{\text{cat}}} \quad (3)$$

$$r_{(\text{styrene})}^* = \frac{C_{\text{styrene}} \times F}{m_{\text{cat}} \times S_{\text{BET}}} \times \ln \left[ \frac{1}{1 - X_{\text{styrene}}} \right] \quad (4)$$

Besides, apparent activation energies ( $E_a$  and  $E_a\text{-norm}$ ) of styrene catalytic oxidation were calculated by the Arrhenius Eqs. (5) and (6). For reaction rates, selecting points where the styrene conversion is less than 15% for estimation.

$$\ln(r_{\text{styrene}}) = -\frac{E_a}{RT} + C \quad (5)$$

$$\ln(r_{\text{styrene}}^*) = -\frac{E_a - \text{norm}}{RT} + C \quad (6)$$

For water-resistant experiments, water vapor at concentrations of 15/10/5 vol% was introduced using a liquid-phase pump with the heating belt heating reaction route. The durability tests were the same as the water resistance test except that without water vapor.

### 2.3. Catalyst characterization and DFT calculations

The prepared  $\text{CeO}_2\text{-(No)C}_8\text{H}_8$  catalysts were characterized by the following characterization methods: X-ray powder diffraction (XRD),  $\text{N}_2$  adsorption-desorption isotherms, transmission electron microscopy (TEM), high-resolution transmission electron microscopy (HRTEM), electron energy loss spectroscopy (EELS), extended X-ray adsorption fine structure (EXAFS) Experiment,  $\text{H}_2$ -TPR,  $\text{O}_2$ -TPD, UV-Raman spectroscopy, X-ray photoelectron spectroscopy (XPS), electron paramagnetic resonance (EPR) spectroscopy, positron annihilation lifetime spectroscopy (PALS), Styrene-TPD, Styrene-TPSR, in-situ Raman, and in-situ DRIFTS. The specific details of all the above characterization methods are listed in the [supplementary information 1.1–1.5](#).

For density function theory (DFT) theoretical calculations, the specific modelling process and methods are shown in the [supplementary information 1.6](#).

## 3. Results and discussion

### 3.1. Synthesis of induced $\text{CeO}_2$

It should be emphasized that the preparation of induced  $\text{CeO}_2$  is based on the idea of "using the spear of styrene to attack the shield of styrene". Briefly, by adding styrene during the preparation of the spherical  $\text{CeO}_2$  catalyst, the structural and morphological properties of  $\text{CeO}_2$  are adjusted by the optimization of the crystallization time and crystallization temperature. This results in the dominant growth of crystalline surfaces that have strong interactions with styrene. In the early stage, we optimized the crystallization time and temperature of induced cerium dioxide using activity experiments. The specific results can be found in the [Fig. S16 of supplementary information](#).

**Table 1**

The summary of physical (XRD, N<sub>2</sub>-adsorption and desorption) and chemical properties (XPS, UV-Raman) of induced CeO<sub>2</sub> catalysts (CeO<sub>2</sub>-C<sub>8</sub>H<sub>8</sub>-130-X, X = 6, 12, 18, and 24).

Samples	FWHM of (111)	CeO <sub>2</sub> Average crystallite size (nm)	BET surface area (m <sup>2</sup> /g)	Pore volume (cm <sup>3</sup> /g)	BJH pore size (nm)	Ce <sup>3+</sup> /(Ce <sup>3+</sup> +Ce <sup>4+</sup> )	O <sub>ads</sub> /(O <sub>ads</sub> +O <sub>latt</sub> +O <sub>OH</sub> )	I <sub>D</sub> /I <sub>G2g</sub>
CeO <sub>2</sub> -C <sub>8</sub> H <sub>8</sub> -130-6	0.86	8.42	156.09	0.15	3.41	20.75%	26.78%	0.33
CeO <sub>2</sub> -C <sub>8</sub> H <sub>8</sub> -130-12	0.87	6.75	192.89	0.42	3.05	24.95%	28.31%	0.42
CeO <sub>2</sub> -C <sub>8</sub> H <sub>8</sub> -130-18	0.83	6.78	142.38	0.10	3.42	25.98%	34.48%	0.47
CeO <sub>2</sub> -C <sub>8</sub> H <sub>8</sub> -130-24	0.90	7.14	163.59	0.10	3.41	29.42%	46.26%	0.73

### 3.2. Structural and morphological analysis

#### 3.2.1. XRD analysis

The XRD patterns of the CeO<sub>2</sub>-C<sub>8</sub>H<sub>8</sub>-130-6, CeO<sub>2</sub>-C<sub>8</sub>H<sub>8</sub>-130-12, CeO<sub>2</sub>-C<sub>8</sub>H<sub>8</sub>-130-18, and CeO<sub>2</sub>-C<sub>8</sub>H<sub>8</sub>-130-24 catalysts are shown in Fig. S1(a). All samples have the cubic fluorite structure of pure CeO<sub>2</sub>, and no other impurity peaks are observed in the patterns. The characteristic peaks of the (111), (200), (220), (311), (222), (400), (331) and (420) planes are located at  $2\theta = 28.5^\circ, 33.1^\circ, 47.5^\circ, 56.3^\circ, 59.1^\circ, 69.4^\circ, 76.7^\circ$  and  $79.1^\circ$  (JCPDS No. 43-1002), respectively. Additionally, CeO<sub>2</sub>-C<sub>8</sub>H<sub>8</sub>-110-24, CeO<sub>2</sub>-C<sub>8</sub>H<sub>8</sub>-120-24 and CeO<sub>2</sub>-NoC<sub>8</sub>H<sub>8</sub>-130-24 show similar peaks (Fig. S1(b) and Fig. S2). CeO<sub>2</sub>-C<sub>8</sub>H<sub>8</sub>-130-24 exhibits broader and shorter XRD diffraction peaks with an increase in crystallization time and temperature, which implies that this catalyst has a more distorted lattice and a smaller grain size. This is favorable for the formation of more oxygen vacancies [13,19]. The peak widths and average crystallite size of the samples were calculated by Jade 6 analysis and are shown in Table 1.

#### 3.2.2. N<sub>2</sub>-adsorption/desorption analysis

As shown in Fig. S3(a), all samples exhibit typical IV isotherms. The CeO<sub>2</sub>-C<sub>8</sub>H<sub>8</sub>-110-24, CeO<sub>2</sub>-C<sub>8</sub>H<sub>8</sub>-120-18, CeO<sub>2</sub>-C<sub>8</sub>H<sub>8</sub>-130-6, CeO<sub>2</sub>-C<sub>8</sub>H<sub>8</sub>-130-12, CeO<sub>2</sub>-C<sub>8</sub>H<sub>8</sub>-130-18, CeO<sub>2</sub>-C<sub>8</sub>H<sub>8</sub>-130-24, CeO<sub>2</sub>-NoC<sub>8</sub>H<sub>8</sub>-130-24 samples show obvious H3 hysteresis loops, indicating that they are mesoporous or microporous materials. In contrast, CeO<sub>2</sub>-C<sub>8</sub>H<sub>8</sub>-120-24 shows an H1 hysteresis loop, an indication that it is a mesoporous material with a relatively narrow pore size distribution or that it consists of uniform spherical particles. The specific surface areas of all the induced CeO<sub>2</sub> samples, determined by N<sub>2</sub> adsorption/desorption analysis, are shown in Table 1 and Table S1. At a crystallization temperature of 130 °C, the specific surface area and pore volume tend to increase and then decrease as the crystallization time increases. The CeO<sub>2</sub>-C<sub>8</sub>H<sub>8</sub>-130-24 catalyst has a BET specific surface area of 163.59 m<sup>2</sup>/g and an average crystallite size of 7.14 nm. And the CeO<sub>2</sub>-C<sub>8</sub>H<sub>8</sub>-130-6 has a BET specific surface area of 156.09 m<sup>2</sup>/g and an average crystallite size of 8.42 nm. In contrast, CeO<sub>2</sub>-NoC<sub>8</sub>H<sub>8</sub>-130-24 has a BET specific surface area of 188.74 m<sup>2</sup>/g and an average crystallite size of 10.89 nm. The results demonstrate that the interaction between the liquid styrene and the CeO<sub>2</sub> crystal surface restricts the growth of ceria nanocrystals.

#### 3.2.3. TEM and HRTEM analysis

The morphologies and lattice fringes of the samples were characterized by TEM and HRTEM (Fig. 2(a) and Fig. S5). The induced CeO<sub>2</sub> evolves from a regular spheroid shape to a rod-like shape as the crystallization time increases, and the exposed crystal surface changes accordingly. As shown by the HRTEM analysis (Fig. S5(a)-(c)), CeO<sub>2</sub>-C<sub>8</sub>H<sub>8</sub>-130-6 mainly exposes (100) and (110) crystalline faces. As the crystallization time increases, the (111) crystalline facet appeared in CeO<sub>2</sub>-C<sub>8</sub>H<sub>8</sub>-130-12. The CeO<sub>2</sub>-C<sub>8</sub>H<sub>8</sub>-130-18 sample exposes many (111) crystalline facets, while CeO<sub>2</sub>-C<sub>8</sub>H<sub>8</sub>-130-24 primarily shows (111) crystalline facets after the crystallization time is extended to 24 h. Analyzing the HRTEM images of CeO<sub>2</sub>-C<sub>8</sub>H<sub>8</sub>-130-24 shows that the

grains have homogeneous interfaces in addition to a similar lattice orientation. It has been reported that a large and homogeneous Ce-Ce interface is conducive to the formation of oxygen vacancies and structural defects (Figs. 2(a-3), Fig. S4(a), (c)). It is still unclear, however, how the abundant interfaces between grains are formed. As demonstrated by the TEM (HRTEM) analysis of these induced CeO<sub>2</sub> samples, the high viscosity of the liquid-phase styrene as an organic solvent reduces the nucleation and growth rate of CeO<sub>2</sub>. This provides the CeO<sub>2</sub> with a more homogeneous and regular morphology. This type of interfacial behavior is not observed for CeO<sub>2</sub>-NoC<sub>8</sub>H<sub>8</sub>-130-24 (prepared without liquid-phase styrene). Even with increasing crystallization time, the CeO<sub>2</sub>-NoC<sub>8</sub>H<sub>8</sub>-130-24 samples expose more (111) crystalline facets (Fig. S6(h-i)), which needs to be further verified by additional testing and characterization. Interestingly, this TEM analysis reveals a process of rod-like formation (Fig. S7), where the initial spherical particles dissociate and slowly assemble into rod-like structures with increasing crystallization time. This is potentially because the 'induction' effect of the liquid styrene may contribute to the surface disorder of CeO<sub>2</sub>-C<sub>8</sub>H<sub>8</sub>-130-24 and the formation of more pronounced interfaces between the grains.

#### 3.2.4. EELS analysis

As shown in Fig. 2(b) and Fig. S8, the HAADF-STEM results are consistent with the HRTEM analysis. CeO<sub>2</sub>-C<sub>8</sub>H<sub>8</sub>-130-24 exhibits abundant lattice defects and blurring. Three areas of the CeO<sub>2</sub>-C<sub>8</sub>H<sub>8</sub>-130-24 catalyst were examined by EELS: the nanosphere at the junction of the nanosphere and the nanorod, the nanosphere alone, and the nanorod alone (Fig. S9). Of these three regions, the highest M<sub>5</sub>/M<sub>4</sub> value is obtained at the nanosphere, followed by a medium M<sub>5</sub>/M<sub>4</sub> value at the junction of the nanosphere and the nanorod. The lowest M<sub>5</sub>/M<sub>4</sub> value is achieved at the nanorod (Fig. 2(c) and Table S2). Thus, it can be speculated that during the spherical dissociation process that forms the nanorods, more CeO<sub>2</sub> (111) crystal facets are exposed in the original spherical shape. This forms more crystal boundaries, resulting in the lattice blurring and lattice distortion of CeO<sub>2</sub>-C<sub>8</sub>H<sub>8</sub>-130-24. In addition, as shown in Fig. S10, obvious interfaces can be observed at the junction of the nanorod and nanosphere in CeO<sub>2</sub>-C<sub>8</sub>H<sub>8</sub>-130-24. As a result, the CeO<sub>2</sub>-C<sub>8</sub>H<sub>8</sub>-130-24 catalyst has abundant Ce-Ce interfaces inside the nanospheres as well as rod-sphere interfaces. Therefore, it can be speculated that liquid styrene can induce the structural evolution of CeO<sub>2</sub> nanocrystals from spheres to short nanorods. The TEM and HAADF-STEM analysis shows that the CeO<sub>2</sub> nanorods possess abundant crystal boundaries and that every grain is freely distributed. The grain boundaries form lattice distortion regions in polycrystals through stabilizing dislocations [34]. The pink circle in Fig. S8 indicates there is a significant distortion at the grain boundaries, resulting in more oxygen vacancies. Previous studies have also shown that lattice distortion favors the creation of oxygen vacancies [13].



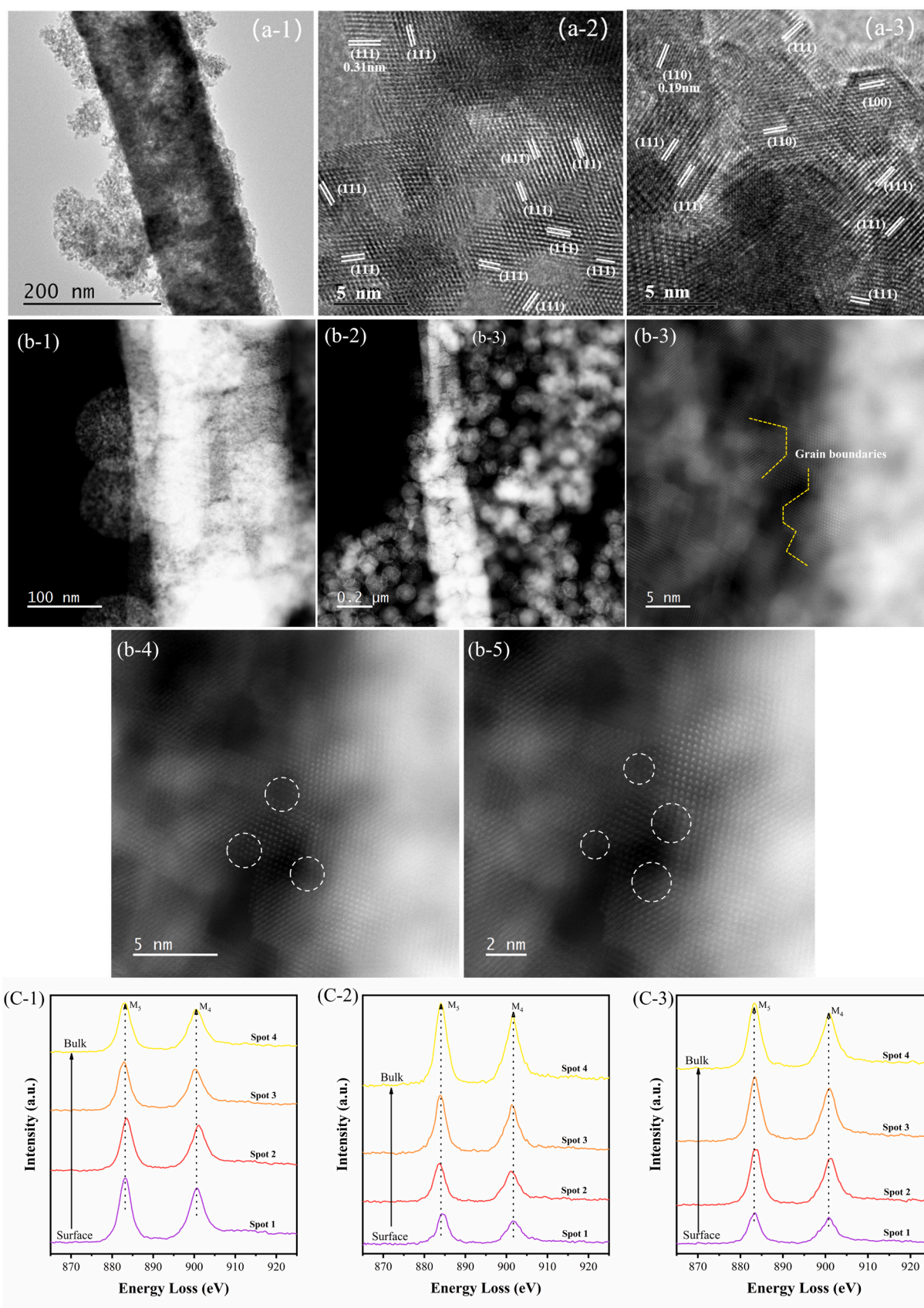


**Fig. 2.** TEM and HRTEM images of (a-1) -(a-3)  $\text{CeO}_2\text{-C}_8\text{H}_8\text{-130-24}$ . (b) STEM HAADF images of  $\text{CeO}_2\text{-C}_8\text{H}_8\text{-130-24}$ . (The white circles represent lattice blurring and lattice defects). (c) O K-edge spectra as function of different position on  $\text{CeO}_2$  (obtained from (Fig. S9)).

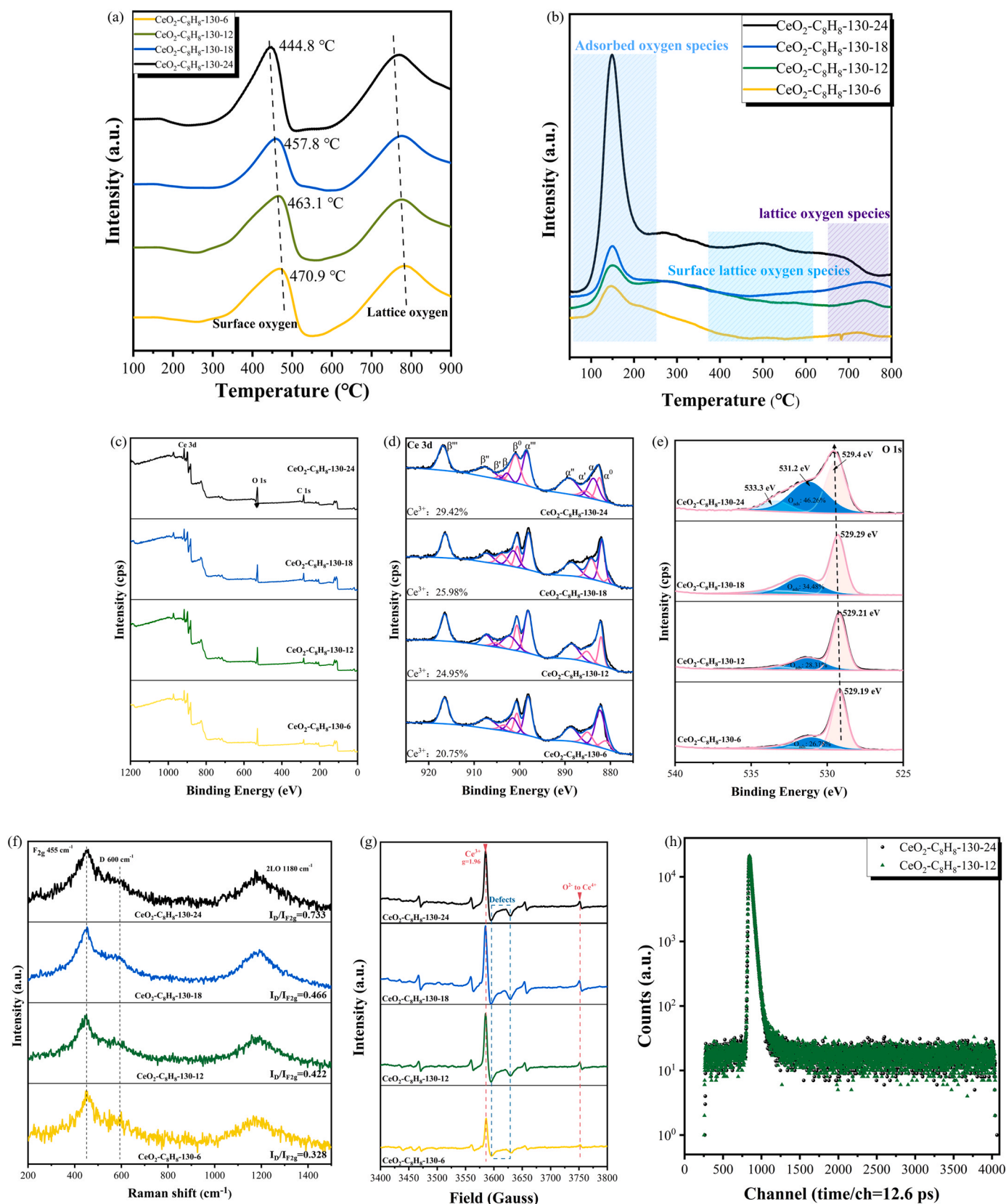


**Fig. 3.** H<sub>2</sub>-TPR profiles of CeO<sub>2</sub>-C<sub>8</sub>H<sub>8</sub>-130-6, CeO<sub>2</sub>-C<sub>8</sub>H<sub>8</sub>-130-12, CeO<sub>2</sub>-C<sub>8</sub>H<sub>8</sub>-130-18 and CeO<sub>2</sub>-C<sub>8</sub>H<sub>8</sub>-130-24. (b) O<sub>2</sub>-TPD Profiles of CeO<sub>2</sub>-C<sub>8</sub>H<sub>8</sub>-130-6, CeO<sub>2</sub>-C<sub>8</sub>H<sub>8</sub>-130-12, CeO<sub>2</sub>-C<sub>8</sub>H<sub>8</sub>-130-18 and CeO<sub>2</sub>-C<sub>8</sub>H<sub>8</sub>-130-24. (c) XPS spectra of all the fresh samples. Full-range scan of the CeO<sub>2</sub>-C<sub>8</sub>H<sub>8</sub>-130-X (X = 6, 12, 18 and 24). (d) Ce 3d spectra of CeO<sub>2</sub>-C<sub>8</sub>H<sub>8</sub>-130-X (X = 6, 12, 18 and 24). (e) O 1s spectra of CeO<sub>2</sub>-C<sub>8</sub>H<sub>8</sub>-130-X (X = 6, 12, 18 and 24). (f) UV-Raman spectra of CeO<sub>2</sub>-C<sub>8</sub>H<sub>8</sub>-130-6, CeO<sub>2</sub>-C<sub>8</sub>H<sub>8</sub>-130-12, CeO<sub>2</sub>-C<sub>8</sub>H<sub>8</sub>-130-18, and CeO<sub>2</sub>-C<sub>8</sub>H<sub>8</sub>-130-24. (g) EPR spectrums of CeO<sub>2</sub>-C<sub>8</sub>H<sub>8</sub>-130-6, CeO<sub>2</sub>-C<sub>8</sub>H<sub>8</sub>-130-12, CeO<sub>2</sub>-C<sub>8</sub>H<sub>8</sub>-130-24, and CeO<sub>2</sub>-NoC<sub>8</sub>H<sub>8</sub>-130-24. (h) PALS spectra of CeO<sub>2</sub>-C<sub>8</sub>H<sub>8</sub>-130-24 and CeO<sub>2</sub>-C<sub>8</sub>H<sub>8</sub>-130-12.

### 3.3. Redox properties

#### 3.3.1. $H_2$ -TPR

In general,  $H_2$ -TPR is used to analyze the redox capabilities of catalysts. During the  $H_2$ -TPR process, both surface oxygen ions and lattice oxygen ions are involved in the reduction reaction. The  $H_2$ -TPR curves of all the prepared induced and non-induced catalysts are shown in Fig. 3 (a) and Fig. S11 (CeO<sub>2</sub>-(No)C<sub>8</sub>H<sub>8</sub>-130-X, CeO<sub>2</sub>-C<sub>8</sub>H<sub>8</sub>-120-X, CeO<sub>2</sub>-C<sub>8</sub>H<sub>8</sub>-110-X). Two obvious reduction peaks that reflect oxygen species activity can be observed. The first reduction peak (in the range of 150–450 °C for all catalysts) can be attributed to adsorbed oxygen species: the superoxide ion O<sub>2</sub><sup>-</sup>. The second reduction peak (450–700 °C) can be assigned to lattice oxygen species: the peroxide ion O<sub>2</sub><sup>2-</sup>/O<sup>2-</sup> [35–37]. As shown in Fig. S11(a), the reduction temperature of the surface oxygen species of the induced CeO<sub>2</sub>-C<sub>8</sub>H<sub>8</sub>-130–24 catalyst (444.8 °C) is shifted to a lower temperature compared with the non-induced CeO<sub>2</sub>-NoC<sub>8</sub>H<sub>8</sub>-130–24 catalyst (469.6 °C). Moreover, the intensities of the two reduction peaks of CeO<sub>2</sub>-C<sub>8</sub>H<sub>8</sub>-130–24 are significantly higher than those of CeO<sub>2</sub>-NoC<sub>8</sub>H<sub>8</sub>-130–24. This indicates that the reducibility of CeO<sub>2</sub>-C<sub>8</sub>H<sub>8</sub>-130–24 is improved by adding styrene. Meanwhile, the two reduction peaks of CeO<sub>2</sub>-C<sub>8</sub>H<sub>8</sub>-130–24 have a larger area than those of the other catalysts. Therefore, the induced CeO<sub>2</sub>-C<sub>8</sub>H<sub>8</sub>-130–24 catalyst exhibits the best reduction performance, which will be beneficial for the catalytic oxidation of styrene.

#### 3.3.2. O<sub>2</sub>-TPD

The oxygen-supplying performance of catalysts is fundamental to their catalytic performance. Therefore, O<sub>2</sub>-TPD was employed to assess the mobility of oxygen species in CeO<sub>2</sub>. The O<sub>2</sub>-TPD profiles of all the induced catalysts are shown in Fig. 3(b) and Fig. S12. For CeO<sub>2</sub>-C<sub>8</sub>H<sub>8</sub>-130–24, a strong peak centered at around 150 °C is due to physically adsorbed oxygen molecules (ads-O<sub>2</sub>) and adsorbed O<sub>2</sub> (ads-O<sub>2</sub>) [38,39]. Some weak peaks in the range of 350–600 °C can be attributed to atom oxygen species (O<sup>-</sup>) or O<sub>2</sub><sup>2-</sup> peroxide ions (surface lattice oxygen) [40]. The peak at higher temperatures (T > 600 °C) is caused by O<sup>2-</sup>, lattice oxygen [41]. For CeO<sub>2</sub>-NoC<sub>8</sub>H<sub>8</sub>-130–24, the first peak (ads-O<sub>2</sub> and ads-O<sub>2</sub>) occurs at 151 °C. Compare with CeO<sub>2</sub>-NoC<sub>8</sub>H<sub>8</sub>-130–24, the peak of CeO<sub>2</sub>-C<sub>8</sub>H<sub>8</sub>-130–24 shows a shift in the low-temperature direction (148 °C). This is caused by the addition of liquid styrene, which changes the electronic properties of CeO<sub>2</sub> and its lattice defects [24]. Meanwhile, there are abundant adsorbed oxygen species and surface lattice oxygen species on the induced CeO<sub>2</sub>-C<sub>8</sub>H<sub>8</sub>-130–24 catalyst. In terms of quantitative analysis, the strength of the adsorbed oxygen species on CeO<sub>2</sub>-C<sub>8</sub>H<sub>8</sub>-130–24 is 1.7 times that of CeO<sub>2</sub>-NoC<sub>8</sub>H<sub>8</sub>-130–24, indicating that the induced CeO<sub>2</sub>-C<sub>8</sub>H<sub>8</sub>-130–24 has abundant oxygen vacancies to promote the adsorption of oxygen molecules in the gas phase. The O<sub>2</sub>-TPD curves of the induced CeO<sub>2</sub> catalysts prepared with different crystallization times are shown in Fig. 3(b). The induced CeO<sub>2</sub>-C<sub>8</sub>H<sub>8</sub>-130–24 catalyst has superior oxygen storage capacity. The peaks associated with the adsorption of oxygen, surface lattice oxygen, and lattice oxygen all have higher intensities in the curve of the induced CeO<sub>2</sub>-C<sub>8</sub>H<sub>8</sub>-130–24 catalyst. Peak intensity follows the order CeO<sub>2</sub>-C<sub>8</sub>H<sub>8</sub>-130–24 > CeO<sub>2</sub>-C<sub>8</sub>H<sub>8</sub>-130–18 > CeO<sub>2</sub>-C<sub>8</sub>H<sub>8</sub>-130–12 > CeO<sub>2</sub>-C<sub>8</sub>H<sub>8</sub>-130–6. Among these samples, the adsorbed oxygen peak area of CeO<sub>2</sub>-C<sub>8</sub>H<sub>8</sub>-130–24 is 5.8 times larger than that of CeO<sub>2</sub>-C<sub>8</sub>H<sub>8</sub>-130–6.

### 3.4. Characterization of oxygen vacancies

#### 3.4.1. XPS

The surface elemental composition of the prepared metal oxide catalysts and the state of their surface oxygen species were analyzed by XPS. The Ce 3d and O 1s XPS spectra of the induced CeO<sub>2</sub>-C<sub>8</sub>H<sub>8</sub>-130-X and CeO<sub>2</sub>-NoC<sub>8</sub>H<sub>8</sub>-130–24 catalysts are shown in Fig. 3(c) and Fig. S13. The Ce 3d spectra were deconvoluted into ten peaks using CasaXPS software. These peaks are denoted  $\alpha^0$  (882.2 eV),  $\alpha$  (883.1 eV),  $\alpha'$  (885.1 eV),  $\alpha''$  (889.3 eV),  $\alpha'''$  (898.4 eV),  $\beta^0$  (899.4 eV),  $\beta$  (900.7 eV),

$\beta'$  (902.2 eV),  $\beta''$  (907.6 eV), and  $\beta'''$  (916.9 eV), where the peaks marked  $\alpha$  and  $\beta$  are assigned to Ce 3d<sub>3/2</sub> and Ce 3d<sub>5/2</sub>, respectively [42]. The peaks labeled  $\alpha^0$ ,  $\alpha'$ ,  $\beta^0$ , and  $\beta'$  are attributed to Ce<sup>3+</sup>, and the peaks labeled  $\alpha$ ,  $\alpha''$ ,  $\alpha'''$ ,  $\beta$ ,  $\beta'$ , and  $\beta'''$  are ascribed to Ce<sup>4+</sup>. Therefore, Ce<sup>3+</sup> and Ce<sup>4+</sup> coexist in all samples. Based on the integrated areas of these peaks (Fig. 3(d)), the (Ce<sup>3+</sup>/(Ce<sup>3+</sup>+Ce<sup>4+</sup>)) ratios of the samples follow the order CeO<sub>2</sub>-C<sub>8</sub>H<sub>8</sub>-130–24 > CeO<sub>2</sub>-C<sub>8</sub>H<sub>8</sub>-130–18 > CeO<sub>2</sub>-C<sub>8</sub>H<sub>8</sub>-130–12 > CeO<sub>2</sub>-C<sub>8</sub>H<sub>8</sub>-130–6 (Table 1). Additionally, the Ce<sup>3+</sup> concentration is higher in the induced CeO<sub>2</sub>-C<sub>8</sub>H<sub>8</sub>-130–24 catalyst (29.42%) than in the non-induced CeO<sub>2</sub>-NoC<sub>8</sub>H<sub>8</sub>-130–24 catalyst (21.75%). Notably, the CeO<sub>2</sub>-C<sub>8</sub>H<sub>8</sub>-130–24 catalyst has a higher percentage of surface Ce<sup>3+</sup> than the other prepared catalysts. There is a positive correlation between the amount of Ce<sup>3+</sup> and the catalytic activity for styrene oxidation, which indicates the formation of non-stoichiometric cerium oxide. The generation of Ce<sup>3+</sup> leads to the corresponding generation of oxygen vacancies, which play an important role in the oxidation process. A surface oxygen vacancy is a more unstable structure with high energy. Thus, lattice oxygen can migrate outward to the surface and fill the empty position of the oxygen vacancy to form a relatively stable structure. This lowers the energy of the unstable structure. Meanwhile, it is widely accepted that the migration of oxygen in CeO<sub>2</sub> takes place via a vacancy hopping mechanism. The presence of more oxygen vacancies accelerates the formation of surface-active oxygen species from activated gas-phase oxygen molecules and promotes the rapid migration of lattice oxygen to the catalyst surface to participate in the reaction.

The O 1s XPS spectra of all the samples are shown in Fig. 3(e). These spectra can be divided into three peaks at 529.5 eV, 531.2 eV, and 533.3 eV, which are assigned to lattice oxygen species (O<sub>latt</sub>), surface adsorbed oxygen species (O<sub>ads</sub>) and adsorbed surface hydroxyl groups (O<sub>adsOH</sub>), respectively [13,18,26]. Based on the integral area of these three peaks, the (O<sub>ads</sub>/(O<sub>ads</sub> + O<sub>latt</sub> + O<sub>adsOH</sub>)) ratio was calculated to reflect the surface adsorbed oxygen species concentration (Table 1). Compared to CeO<sub>2</sub>-C<sub>8</sub>H<sub>8</sub>-130–6 (26.78%), CeO<sub>2</sub>-C<sub>8</sub>H<sub>8</sub>-130–12 (28.31%), and CeO<sub>2</sub>-C<sub>8</sub>H<sub>8</sub>-130–18 (34.48%), CeO<sub>2</sub>-C<sub>8</sub>H<sub>8</sub>-130–24 (46.26%) has a higher (O<sub>ads</sub>/(O<sub>ads</sub> + O<sub>latt</sub> + O<sub>adsOH</sub>)) ratio, suggesting that CeO<sub>2</sub>-C<sub>8</sub>H<sub>8</sub>-130–24 has a higher level of surface adsorbed oxygen species. Additionally, the O<sub>latt</sub> peak of CeO<sub>2</sub>-C<sub>8</sub>H<sub>8</sub>-130–24 is slightly shifted to a higher binding energy, indicating a lower electron cloud density around the O<sub>latt</sub> and a higher mobility of the lattice oxygen species [43].

#### 3.4.2. UV-Raman

The UV-Raman spectra of the prepared samples are shown in Fig. 3 (f). The strongest peak is located at a wavenumber of approximately 455 cm<sup>-1</sup>, corresponding to the symmetric stretching vibrations of the I<sub>F2g</sub> mode of the CeO<sub>2</sub> lattice [44]. In addition, there is a weak peak at about 600 cm<sup>-1</sup> associated with the defected-induced I<sub>D</sub> mode caused by oxygen vacancies in the presence of Ce<sup>3+</sup>. The I<sub>D</sub>/I<sub>F2g</sub> intensity ratio was used to estimate the oxygen vacancy concentrations of the samples, which follow the order: CeO<sub>2</sub>-C<sub>8</sub>H<sub>8</sub>-130–24 (0.733) > CeO<sub>2</sub>-C<sub>8</sub>H<sub>8</sub>-130–18 (0.466) > CeO<sub>2</sub>-C<sub>8</sub>H<sub>8</sub>-130–12 (0.422) > CeO<sub>2</sub>-C<sub>8</sub>H<sub>8</sub>-130–6 (0.328) (Table 1). For comparison (Fig. S14), the I<sub>D</sub>/I<sub>F2g</sub> ratio of CeO<sub>2</sub>-NoC<sub>8</sub>H<sub>8</sub>-130–24 (0.605) was also calculated. This I<sub>D</sub>/I<sub>F2g</sub> ratio is lower than that of CeO<sub>2</sub>-C<sub>8</sub>H<sub>8</sub>-130–24. Overall, the  $H_2$ -TPR, O<sub>2</sub>-TPD, XPS, and UV-Raman characterization appears to be consistent and corroborated.

#### 3.4.3. EPR

EPR analysis was used to evaluate the Ce species and oxygen vacancies in the CeO<sub>2</sub> samples. As shown in Fig. 3(g), the field at 3600–3625 Gauss is assigned to a surface oxygen vacancy, and the g = 1.96 band is attributed to Ce<sup>3+</sup> [13,44]. These results show that CeO<sub>2</sub>-C<sub>8</sub>H<sub>8</sub>-130–24 and CeO<sub>2</sub>-C<sub>8</sub>H<sub>8</sub>-130–18 have the largest proportion of oxygen vacancies among the induced CeO<sub>2</sub>-C<sub>8</sub>H<sub>8</sub> catalysts. This is consistent with the XPS and UV-Raman results. EPR can only detect a single oxygen vacancy. Thus, oxygen vacancy clusters cannot be reflected in the signal [45]. This means that EPR spectroscopy is unable to identify the difference in oxygen vacancy content between



CeO<sub>2</sub>-C<sub>8</sub>H<sub>8</sub>-130-24 and CeO<sub>2</sub>-NoC<sub>8</sub>H<sub>8</sub>-130-24. This phenomenon suggests that CeO<sub>2</sub>-C<sub>8</sub>H<sub>8</sub>-130-24 may have more oxygen vacancy clusters.

### 3.4.4. PALS

The distribution of oxygen vacancies was characterized by PALS, as shown in Fig. 3(h) and Table S3. As described in previous studies, a multi-exponential function was used to deconvolute the spectrum into three different lifetime components. In general, the positron lifetime is strongly influenced by the electron density at the annihilation point, and this lifetime increases with decreasing electron density. For CeO<sub>2</sub> catalysts, it has been shown that the shortest component  $\tau_1$  reflects free positron annihilation either in a perfect lattice (when  $\tau_1 < 0.187$  ns) or when trapped by monodisperse oxygen vacancies in the bulk structure (when  $\tau_1 > 0.187$  ns). The intermediate lifetime component  $\tau_2$  is assigned to the annihilation of positrons trapped by oxygen vacancy clusters. The longest lifetime component  $\tau_3$  is attributed to the annihilation of positive ion atoms that occurs at the large voids between nanoparticles [26,36]. Therefore, the  $\tau_1$  value of CeO<sub>2</sub>-C<sub>8</sub>H<sub>8</sub>-130-24 indicates the annihilation of positrons trapped by monodisperse oxygen vacancies in the bulk, while that of CeO<sub>2</sub>-C<sub>8</sub>H<sub>8</sub>-130-12 indicates the free positron annihilation in a perfect lattice. Hence, CeO<sub>2</sub>-C<sub>8</sub>H<sub>8</sub>-130-24 has a higher number of bulk oxygen vacancies than CeO<sub>2</sub>-C<sub>8</sub>H<sub>8</sub>-130-12. Furthermore, the relative intensities of specific lifetime components are closely related to the oxygen vacancy concentration. CeO<sub>2</sub>-C<sub>8</sub>H<sub>8</sub>-130-24 has a higher  $I_1$  value than CeO<sub>2</sub>-C<sub>8</sub>H<sub>8</sub>-130-12, indicating that CeO<sub>2</sub>-C<sub>8</sub>H<sub>8</sub>-130-24 has more monodisperse oxygen vacancies in the bulk than CeO<sub>2</sub>-C<sub>8</sub>H<sub>8</sub>-130-12. Meanwhile, CeO<sub>2</sub>-C<sub>8</sub>H<sub>8</sub>-130-24 has a higher  $\tau_2$  value than CeO<sub>2</sub>-C<sub>8</sub>H<sub>8</sub>-130-12, indicating more oxygen vacancy clusters on the surface of CeO<sub>2</sub>-C<sub>8</sub>H<sub>8</sub>-130-24.

### 3.4.5. XANES

Furthermore, the synthetic structures (local structural environment around Ce atoms) of CeO<sub>2</sub>-C<sub>8</sub>H<sub>8</sub>-130-24 and CeO<sub>2</sub>-C<sub>8</sub>H<sub>8</sub>-130-12 were further investigated using Extended X-ray Absorption Fine Structure (EXAFS) techniques [26,46]. As shown in Fig. S15, both CeO<sub>2</sub>-C<sub>8</sub>H<sub>8</sub>-130-24 and CeO<sub>2</sub>-C<sub>8</sub>H<sub>8</sub>-130-12 demonstrate Fourier-transform  $k^2$ -weighted EXAFS spectra and wavelet transform spectra that are similar to the standard CeO<sub>2</sub> sample. Furthermore, the Ce-Ce bond oscillation in CeO<sub>2</sub>-C<sub>8</sub>H<sub>8</sub>-130-24 was weaker compared to CeO<sub>2</sub>-C<sub>8</sub>H<sub>8</sub>-130-12 in the  $k^2$ -weighted Fourier-transform EXAFS spectra. In the wavelet transform contour plot, CeO<sub>2</sub>-C<sub>8</sub>H<sub>8</sub>-130-24 and CeO<sub>2</sub>-C<sub>8</sub>H<sub>8</sub>-130-12 exhibit two distinct shell maxima attributed to the Ce-O bond in the first shell ( $R \sim 1.8$  Å,  $k \sim 3.5$  Å<sup>-1</sup>) and the Ce-Ce bond in the second shell ( $R \sim 3.7$  Å,  $k \sim 8.2$  Å<sup>-1</sup>) [46]. However, the strength of the Ce-Ce bond is slightly attenuated in CeO<sub>2</sub>-C<sub>8</sub>H<sub>8</sub>-130-24 compared to CeO<sub>2</sub>-C<sub>8</sub>H<sub>8</sub>-130-12. Correspondingly, the coordination numbers of Ce-O and Ce-Ce of CeO<sub>2</sub>-C<sub>8</sub>H<sub>8</sub>-130-24 are lower than CeO<sub>2</sub>-C<sub>8</sub>H<sub>8</sub>-130-12 (Table 2). Based on the results from HRTEM, EELS, UV-Raman, EPR, and PALS, the analysis using EXAFS further confirms that the presence of abundant Ce-Ce grain boundaries in CeO<sub>2</sub>-C<sub>8</sub>H<sub>8</sub>-130-24 causes distortion in the lattice of cerium dioxide crystals. This distortion is due to stable dislocations, which leads to an increased number of oxygen vacancies and prevents multiple scattering of photoelectrons.

**Table 2**  
EXAFS fitting parameters at the Ce L3-edge for various samples.

	shell	CN <sup>a</sup>	R (Å) <sup>b</sup>	$\sigma^2$ <sup>c</sup>	$\Delta E_0$ <sup>d</sup>	R factor <sup>e</sup>
CeO <sub>2</sub> -C <sub>8</sub> H <sub>8</sub> -130-24	Ce-O	5.4 ± 0.5	2.32 ± 0.02	0.0082	6.0 ± 1.7	0.0197
	Ce-Ce	0.6 ± 0.4	3.40 ± 0.05	0.0013		
	Ce-Ce1	3.2 ± 0.6	3.85 ± 0.02	0.0013		
CeO <sub>2</sub> -C <sub>8</sub> H <sub>8</sub> -130-12	Ce-O	5.6 ± 0.4	2.32 ± 0.02	0.0089	5.9 ± 1.5	0.0153
	Ce-Ce	0.6 ± 0.4	3.41 ± 0.04	0.0017		

<sup>a</sup>N: coordination numbers; <sup>b</sup>R: bond distance; <sup>c</sup> $\sigma^2$ : Debye-Waller factors; <sup>d</sup> $\Delta E_0$ : the inner potential correction. R factor: goodness of fit.

## 3.5. Catalytic performance

The catalytic performance of the induced and non-induced CeO<sub>2</sub> catalysts was tested for the catalytic oxidation of styrene to verify the effect of adding styrene on the CeO<sub>2</sub> crystallization process and to gain further insight into the structure-performance relationship of these catalysts. Fig. S16 illustrates the catalytic oxidation performance of the CeO<sub>2</sub> catalysts at low styrene concentrations in the pre-probe stage. The T<sub>90</sub> of these catalysts follow the order CeO<sub>2</sub>-NoC<sub>8</sub>H<sub>8</sub>-130-24 (223 °C) > CeO<sub>2</sub>-C<sub>8</sub>H<sub>8</sub>-130-24 (149 °C). More details are provided in the [supplementary information](#). To further evaluate the activity of the induced catalysts in more detail, 600 ppm styrene was selected as a high-concentration reaction condition to evaluate the catalytic activity.

### 3.5.1. Catalytic performance in styrene oxidation

Fig. 4(a) illustrates the removal of styrene at 30–350 °C. The CeO<sub>2</sub>-C<sub>8</sub>H<sub>8</sub>-130-24 catalyst exhibits superior styrene oxidation conversion compared with the other induced CeO<sub>2</sub>-C<sub>8</sub>H<sub>8</sub> catalysts. Fig. S17(a)–(d) shows the catalytic oxidation at various crystallization temperatures (140 °C, 130 °C, 120 °C, and 110 °C). The effect of crystallization time was also investigated. With increasing crystallization time and crystallization temperature, the catalytic oxidation of styrene gradually increases. The T<sub>50</sub> and T<sub>90</sub> values of the induced CeO<sub>2</sub>-C<sub>8</sub>H<sub>8</sub> catalysts are listed in Table 3 and Table S4. The T<sub>90</sub> values follow the order: CeO<sub>2</sub>-C<sub>8</sub>H<sub>8</sub>-120-18 (244 °C) > CeO<sub>2</sub>-C<sub>8</sub>H<sub>8</sub>-130-6 (222 °C) > CeO<sub>2</sub>-C<sub>8</sub>H<sub>8</sub>-110-24 (219 °C) > CeO<sub>2</sub>-C<sub>8</sub>H<sub>8</sub>-140-36 (220 °C) = CeO<sub>2</sub>-C<sub>8</sub>H<sub>8</sub>-140-24 (220 °C) > CeO<sub>2</sub>-C<sub>8</sub>H<sub>8</sub>-130-48 (217 °C) > CeO<sub>2</sub>-C<sub>8</sub>H<sub>8</sub>-130-36 (213 °C) > CeO<sub>2</sub>-C<sub>8</sub>H<sub>8</sub>-120-24 (208 °C) > CeO<sub>2</sub>-C<sub>8</sub>H<sub>8</sub>-130-12 (198 °C) > CeO<sub>2</sub>-NoC<sub>8</sub>H<sub>8</sub>-130-24 (194 °C) > CeO<sub>2</sub>-C<sub>8</sub>H<sub>8</sub>-130-18 (176 °C) > CeO<sub>2</sub>-C<sub>8</sub>H<sub>8</sub>-130-24 (149 °C). It can be observed that catalytic activity declines below 100 °C and increases with increasing temperature above 100 °C. All the induced CeO<sub>2</sub>-C<sub>8</sub>H<sub>8</sub> catalysts can remove styrene with almost 100% efficiency at about 250 °C. To further demonstrate the advantages of the induced CeO<sub>2</sub>-C<sub>8</sub>H<sub>8</sub> catalysts for the catalytic oxidation of styrene, a comparison of the activity of the induced and non-induced catalysts prepared with crystallization times of 24 and 12 h is provided in Fig. S17 (f). The induced catalysts exhibit better catalytic oxidation activity than the non-induced catalysts. Therefore, the induced catalysts can efficiently degrade styrene by regulating the crystallization temperature and crystallization time. At high temperatures, styrene can undergo self-polymerization. When the crystallization temperature is increased to 140 °C, the catalytic activity decreases significantly. Even at a crystallization temperature of 130 °C, the crystallization time is extended to 48 h. Compared to CeO<sub>2</sub>-C<sub>8</sub>H<sub>8</sub>-130-24, the catalytic activity of CeO<sub>2</sub>-C<sub>8</sub>H<sub>8</sub>-130-36 and CeO<sub>2</sub>-C<sub>8</sub>H<sub>8</sub>-130-48 show a certain degree of decline, especially at 48 h. This suggests that at higher temperatures or longer crystallization times, the added liquid-phase styrene may not fully function as a surfactant due to self-polymerization. As a result, it fails to form a more abundant Ce-Ce crystal boundaries, which is important for catalytic oxidation of styrene. Therefore, by adding liquid styrene as a surfactant, it increases the viscosity of the solution during crystallization. This slows down the rate of crystal formation and promotes the formation of Ce-Ce grain boundaries. And this also helps to create more oxygen vacancies. Compared to other surfactants like CTAB and SDS, styrene as a surfactant in the preparation of cerium dioxide shows better



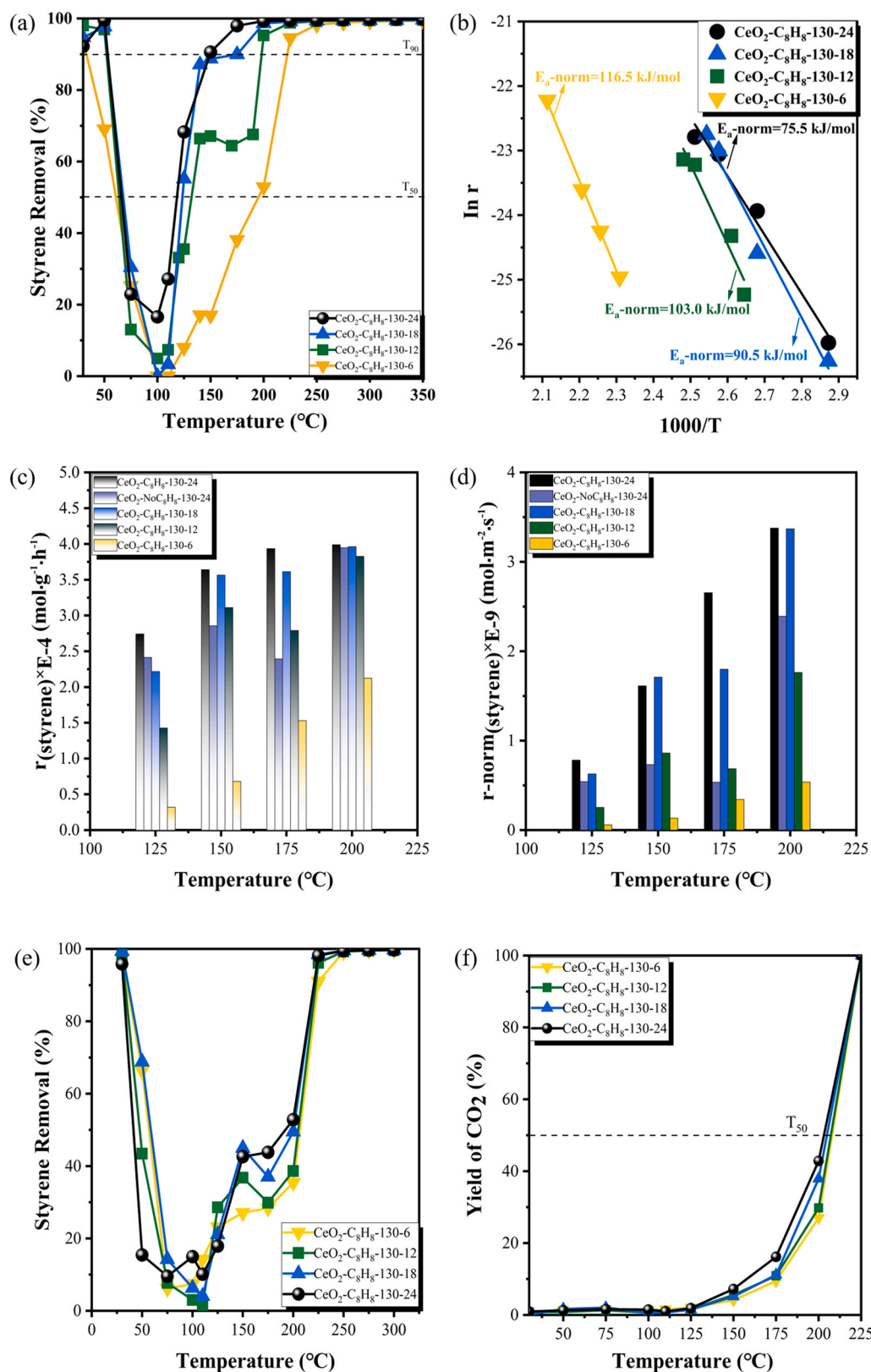


**Fig. 4.** (a) Removal of high concentration (600 ppm) of styrene by induced  $\text{CeO}_2$  catalysts ( $\text{CeO}_2\text{-C}_8\text{H}_8\text{-130-X}$  (X = 6, 12, 18 and 24)). (b) Arrhenius plot of a series of induced  $\text{CeO}_2$  catalysts ( $\text{CeO}_2\text{-C}_8\text{H}_8\text{-130-X}$  (X = 6, 12, 18 and 24)): Normalized by specific surface area. (c) Induced  $\text{CeO}_2$  ( $\text{CeO}_2\text{-C}_8\text{H}_8\text{-130-X}$  (X = 6, 12, 18 and 24)) and  $\text{CeO}_2\text{-NoC}_8\text{H}_8\text{-130-24}$  reaction rates at 125–200 °C. (d) Induced  $\text{CeO}_2$  ( $\text{CeO}_2\text{-C}_8\text{H}_8\text{-130-X}$  (X = 6, 12, 18 and 24)) and  $\text{CeO}_2\text{-NoC}_8\text{H}_8\text{-130-24}$  normalized reaction rates by specific surface area at 125–200 °C. (e) Removal of high concentration (600 ppm) of styrene by induced  $\text{CeO}_2$  catalysts ( $\text{CeO}_2\text{-C}_8\text{H}_8\text{-130-X}$  (X = 6, 12, 18 and 24)) with high WHSV (30,000 mL/(g·h)). (f) Yield of  $\text{CO}_2$  of high concentration (600 ppm) of styrene by induced  $\text{CeO}_2$  catalysts ( $\text{CeO}_2\text{-C}_8\text{H}_8\text{-130-X}$  (X = 6, 12, 18 and 24)) in high WHSV (30,000 mL/(g·h)).

**Table 3**A series of inducible and non-inducible CeO<sub>2</sub> data of catalytic activity and kinetic reaction rates.

Samples	T <sub>50</sub> (°C)	T <sub>90</sub> (°C)	T <sub>50</sub> (°C) <sup>a</sup> with water vapor	T <sub>90</sub> (°C) <sup>b</sup> with water vapor	T <sub>50</sub> (°C) in 30,000 mL/(g·h)	r (styrene) <sup>c</sup> (175 °C)	r * (styrene) <sup>d</sup> (175 °C)	E <sub>a</sub> <sup>e</sup> (kJ·mol <sup>-1</sup> )	E <sub>a</sub> -norm <sup>f</sup> (kJ·mol <sup>-1</sup> )
CeO <sub>2</sub> -C <sub>8</sub> H <sub>8</sub> -130-24	119	149	136	169	191	3.94E-04	2.66E-09	74.50	75.50
CeO <sub>2</sub> -C <sub>8</sub> H <sub>8</sub> -130-18	124	176	150	175	200	3.61E-04	1.80E-09	89.50	90.50
CeO <sub>2</sub> -C <sub>8</sub> H <sub>8</sub> -130-12	132	198	153	174	204	2.79E-04	0.69E-09	101.20	103.00
CeO <sub>2</sub> -C <sub>8</sub> H <sub>8</sub> -130-6	195	222	157	184	207	1.53 E-04	0.34E-09	113.40	116.50

<sup>a</sup> T<sub>50</sub> means the reaction temperature corresponding to the styrene catalytic oxidation conversion of 50%.<sup>b</sup> T<sub>90</sub> means the reaction temperature corresponding to the styrene catalytic oxidation conversion of 90%.<sup>c</sup> r(styrene) means the reaction rate for styrene catalytic oxidation at 175 °C. Calculated from reaction Eq. (3).<sup>d</sup> r \* (styrene) means the normalized reaction rate by surface area for styrene catalytic oxidation at 175 °C. Calculated from reaction Eq. (4).<sup>e</sup> E<sub>a</sub> means the apparent activation energy and was calculated from reaction Eq. (5).<sup>f</sup> E<sub>a</sub> means the normalized reaction rate by surface area for the apparent activation energy and was calculated from reaction Eq. (6).

catalytic activity for styrene and achieves the concept of "using the spear of styrene to attack the shield of styrene" (Fig. S17(h)). Furthermore, CeO<sub>2</sub>-C<sub>8</sub>H<sub>8</sub>-130-24 has excellent catalytic activity for styrene oxidation compared to other catalysts reported in the literature (Table S5) and compared to commercial nano CeO<sub>2</sub> (T<sub>90</sub> = 252 °C).

### 3.5.2. Apparent activation energy and reaction rates

To investigate the kinetics of styrene oxidation over the induced catalysts, their apparent activation energy (E<sub>a</sub>) values were calculated with Arrhenius plots (styrene conversion <15%), which are shown in Fig. 4(b), Fig. S18(a) and Table 3. These E<sub>a</sub> values follow the order CeO<sub>2</sub>-C<sub>8</sub>H<sub>8</sub>-130-6 (113.4 kJ·mol<sup>-1</sup>) > CeO<sub>2</sub>-C<sub>8</sub>H<sub>8</sub>-130-12 (101.2 kJ·mol<sup>-1</sup>) > CeO<sub>2</sub>-C<sub>8</sub>H<sub>8</sub>-130-18 (89.5 kJ·mol<sup>-1</sup>) > CeO<sub>2</sub>-C<sub>8</sub>H<sub>8</sub>-130-24 (74.5 kJ·mol<sup>-1</sup>). Thus, CeO<sub>2</sub>-C<sub>8</sub>H<sub>8</sub>-130-24 has the lowest E<sub>a</sub> value, indicating that the catalytic oxidation of styrene proceeds more easily over this catalyst. Because the catalysts have different surface areas, their E<sub>a</sub> values were normalized in terms of specific surface area, resulting in the same order: CeO<sub>2</sub>-C<sub>8</sub>H<sub>8</sub>-130-6 (116.5 kJ·mol<sup>-1</sup>) > CeO<sub>2</sub>-C<sub>8</sub>H<sub>8</sub>-130-12 (103.0 kJ·mol<sup>-1</sup>) > CeO<sub>2</sub>-C<sub>8</sub>H<sub>8</sub>-130-18 (90.5 kJ·mol<sup>-1</sup>) > CeO<sub>2</sub>-C<sub>8</sub>H<sub>8</sub>-130-24 (75.5 kJ·mol<sup>-1</sup>). After normalizing the reaction rates by specific surface area, the order of E<sub>a</sub> values remains unchanged, indicating that CeO<sub>2</sub>-C<sub>8</sub>H<sub>8</sub>-130-24 exhibits the best catalytic oxidation of styrene because it has the lowest activation energy. In addition, the catalytic performance of the induced and non-induced CeO<sub>2</sub>-C<sub>8</sub>H<sub>8</sub> catalysts was quantified based on reaction rates in the temperature range of 125–200 °C (Fig. 4(c)-(d), Fig. S18 (b)-(c), and Table 3). As shown in Fig. 4(c)-(d), the reaction rates of CeO<sub>2</sub>-C<sub>8</sub>H<sub>8</sub>-130-24, CeO<sub>2</sub>-C<sub>8</sub>H<sub>8</sub>-130-18 and CeO<sub>2</sub>-C<sub>8</sub>H<sub>8</sub>-130-6 catalysts increase with increasing temperature, while the CeO<sub>2</sub>-C<sub>8</sub>H<sub>8</sub>-130-12 catalyst shows a decreasing trend at 175 °C followed by a gradual increase, consistent with Fig. 4(a) (catalytic performance). Furthermore, CeO<sub>2</sub>-NoC<sub>8</sub>H<sub>8</sub>-130-24 also shows an increasing and decreasing reaction rate trend. The reaction rates of this catalyst are significantly lower than those of CeO<sub>2</sub>-C<sub>8</sub>H<sub>8</sub>-130-24 (Fig. 4 (c)). A comparison of the reaction rates after normalizing by specific surface area was also conducted to determine the effect of specific surface area on adsorption sites (Fig. 4(d)). This comparison shows that the normalized reaction rates of the induced CeO<sub>2</sub>-C<sub>8</sub>H<sub>8</sub>-130-24 catalyst are all higher than those of the non-induced CeO<sub>2</sub> catalyst (CeO<sub>2</sub>-NoC<sub>8</sub>H<sub>8</sub>-130-24) in the temperature range of 150–200 °C. Even after normalizing by specific surface area, the reaction rates at 125, 175, and 200 °C follow the order CeO<sub>2</sub>-C<sub>8</sub>H<sub>8</sub>-130-24 > CeO<sub>2</sub>-C<sub>8</sub>H<sub>8</sub>-130-18 > CeO<sub>2</sub>-C<sub>8</sub>H<sub>8</sub>-130-12 > CeO<sub>2</sub>-C<sub>8</sub>H<sub>8</sub>-130-6. This is consistent with the order of activity. Hence, whether the reaction rate is normalized to the specific surface area or not, CeO<sub>2</sub>-C<sub>8</sub>H<sub>8</sub>-130-24 shows an obvious advantage for enhancing the styrene oxidation reaction rate. In summary, the reaction kinetics reveal that CeO<sub>2</sub>-C<sub>8</sub>H<sub>8</sub>-130-24 has the lowest apparent activation energy and the

fastest reaction rate for the catalytic oxidation of styrene because of its abundant Ce-Ce grain boundaries, higher oxygen vacancy concentration, indicating that this catalyst has excellent catalytic performance.

### 3.5.3. Catalytic activity in the presence of water vapor

The catalytic activity of CeO<sub>2</sub>-C<sub>8</sub>H<sub>8</sub>-130-6, CeO<sub>2</sub>-C<sub>8</sub>H<sub>8</sub>-130-12, CeO<sub>2</sub>-C<sub>8</sub>H<sub>8</sub>-130-18, and CeO<sub>2</sub>-C<sub>8</sub>H<sub>8</sub>-130-24 in the presence of 10 vol% water vapor is displayed in Fig. S19. The relevant T<sub>90</sub> and T<sub>50</sub> data are listed in Table 3. To further evaluate the activity of induced CeO<sub>2</sub> at different crystallization times (styrene concentration = 600 ppm, WHSV = 30,000 mL/(g·h)), the temperature-dependent styrene conversion and the CO<sub>2</sub> yields of these CeO<sub>2</sub>-C<sub>8</sub>H<sub>8</sub>-130-X catalysts are displayed in Fig. 4 (e)-(f). CeO<sub>2</sub>-C<sub>8</sub>H<sub>8</sub>-130-24 still exhibits the best catalytic performance and an excellent CO<sub>2</sub> yield for styrene oxidation. For the induced CeO<sub>2</sub>-C<sub>8</sub>H<sub>8</sub> catalysts, the styrene is completely mineralized into CO<sub>2</sub> at 225 °C.

Based on the above analysis of the physical properties (XRD and N<sub>2</sub>-adsorption/desorption analysis) of the induced and non-induced CeO<sub>2</sub> catalysts, it can be concluded that the grain size, specific surface area, and pore size are not key factors affecting their catalytic activity. Moreover, according to XPS, UV-Raman, EPR, H<sub>2</sub>-TPR, O<sub>2</sub>-TPD and other characterization methods, the induced CeO<sub>2</sub>-C<sub>8</sub>H<sub>8</sub>-130-24 catalyst with rich crystal boundaries has the highest oxygen vacancy concentration, excellent redox performance, and the best oxygen storage capacity. This demonstrates the importance of oxygen vacancies in styrene catalytic oxidation.

## 3.6. Reaction mechanism

### 3.6.1. Styrene-TPD and Styrene-TPSR

To further compare the adsorption and oxidation capacities of the induced and non-induced catalysts towards styrene, styrene-TPD and styrene-TPSR were performed. As shown in Fig. 5(a) and Fig. S20 (a)-(d), the peak areas of styrene are reported as a function of temperature. Several adsorbed states of styrene can be observed on the surface of the catalysts. Styrene-TPD suggests that styrene exists in two adsorbed states on the surface of the catalysts. The large main peak at 69 °C is attributed to strong physically adsorbed styrene. Fig. S20(a) shows that CeO<sub>2</sub>-C<sub>8</sub>H<sub>8</sub>-130-24 has a higher adsorption capacity for styrene than CeO<sub>2</sub>-NoC<sub>8</sub>H<sub>8</sub>-130-24. The presence of a shoulder peak at 105.5 °C for the CeO<sub>2</sub>-C<sub>8</sub>H<sub>8</sub>-130-24 catalyst is ascribed to weak chemically adsorbed styrene [39]. There is no obvious shoulder peak on the other catalysts, showing that the chemisorption of styrene is much easier on the CeO<sub>2</sub>-C<sub>8</sub>H<sub>8</sub>-130-24 catalyst. Additionally, one intermediate can be detected during the degradation process. Compared to CeO<sub>2</sub>-NoC<sub>8</sub>H<sub>8</sub>-130-24 and CeO<sub>2</sub>-C<sub>8</sub>H<sub>8</sub>-130-18/12/6, CeO<sub>2</sub>-C<sub>8</sub>H<sub>8</sub>-130-24 produces a smaller amount of intermediate, and this intermediate appears at lower temperatures than the intermediate of the other catalysts (Fig. S20

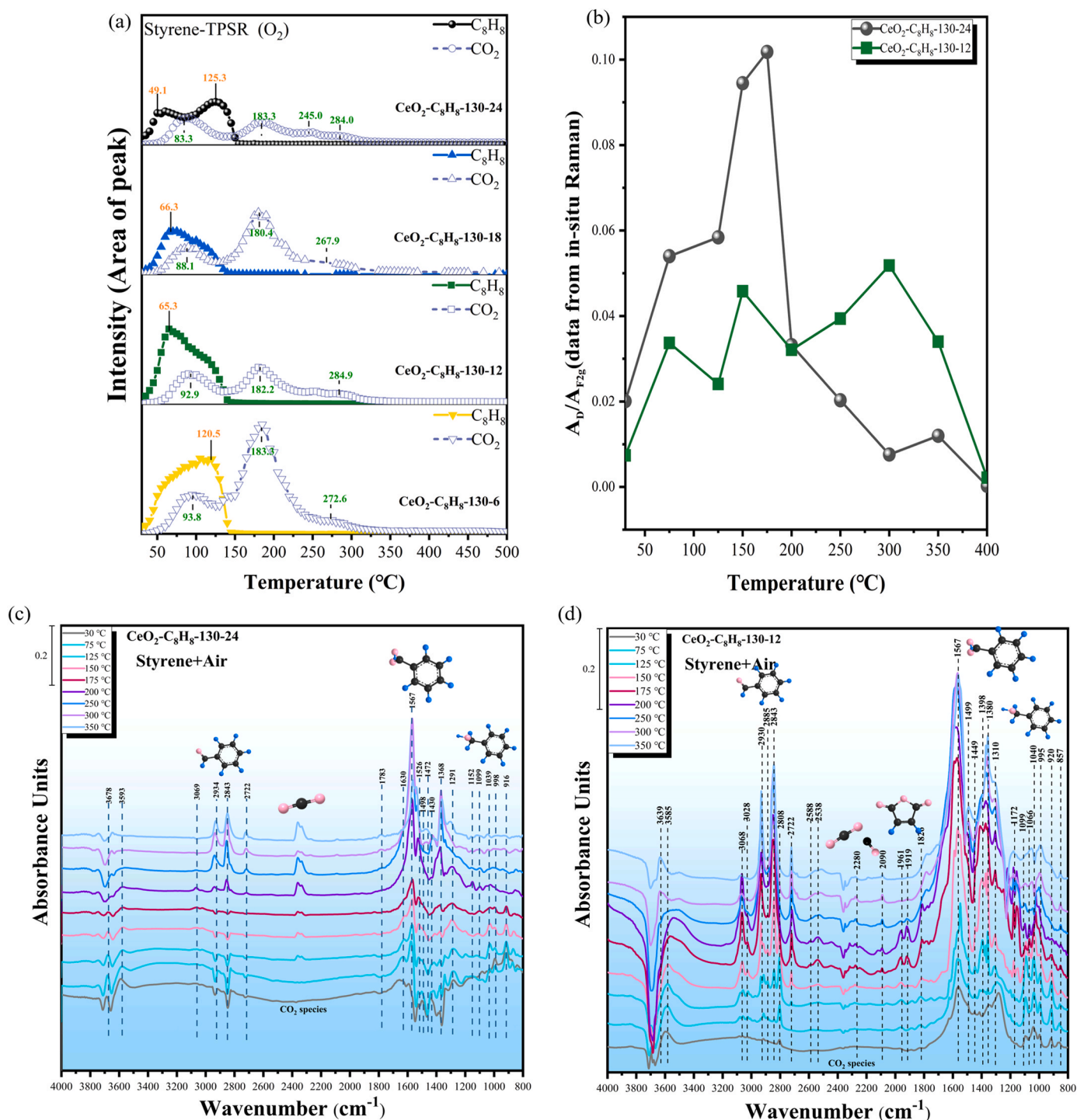


**Fig. 5.** (a) Styrene-TPSR profiles of CeO<sub>2</sub>-C<sub>8</sub>H<sub>8</sub>-130-6, CeO<sub>2</sub>-C<sub>8</sub>H<sub>8</sub>-130-12, CeO<sub>2</sub>-C<sub>8</sub>H<sub>8</sub>-130-18, and CeO<sub>2</sub>-C<sub>8</sub>H<sub>8</sub>-130-24. (b) In-situ Raman spectrum of CeO<sub>2</sub>-C<sub>8</sub>H<sub>8</sub>-130-12 and CeO<sub>2</sub>-C<sub>8</sub>H<sub>8</sub>-130-24. In-situ DRIFTS of styrene oxidation over (c) CeO<sub>2</sub>-C<sub>8</sub>H<sub>8</sub>-130-24. (d) CeO<sub>2</sub>-C<sub>8</sub>H<sub>8</sub>-130-12 under a series of temperatures (30–350 °C).

(b)). Based on the literature [13], the chromatographic column characteristics (polar column) and the retention time of the intermediate, as well as the GC-MS results of the 15-minute exhaust collected at three different temperature points (370, 390, and 410 °C) in the Styrene-TPD process, the intermediate can be further speculated as acetic acid (Fig. S21). These phenomena indicate that the adsorbed styrene on the catalyst is oxidized by the lattice oxygen species, which migrate outward and are activated as the temperature increases. However, some intermediates are observed because they cannot be deeply oxidized. Based on H<sub>2</sub>-TPR and O<sub>2</sub>-TPD analysis, CeO<sub>2</sub>-C<sub>8</sub>H<sub>8</sub>-130-24 demonstrates

abundant surface and lattice oxygen species, and the lattice oxygen is more likely to migrate and participate in the catalytic oxidation process.

Styrene-TPSR was performed on CeO<sub>2</sub>-C<sub>8</sub>H<sub>8</sub>-130-X in the presence of gas-phase oxygen molecules to compare the prepared catalysts in terms of their styrene adsorption and oxidation capacity. As displayed in Fig. 5 (a), similar styrene desorption behavior and oxidation behavior can be observed over the four catalysts from 30° to 500°C. CeO<sub>2</sub>-C<sub>8</sub>H<sub>8</sub>-130-24 exhibits two strong desorption peaks detected at 49.1 and 125.3 °C, which are attributed to strong physically and weak chemically adsorbed styrene, respectively. Moreover, the first CO<sub>2</sub> production peak of CeO<sub>2</sub>-

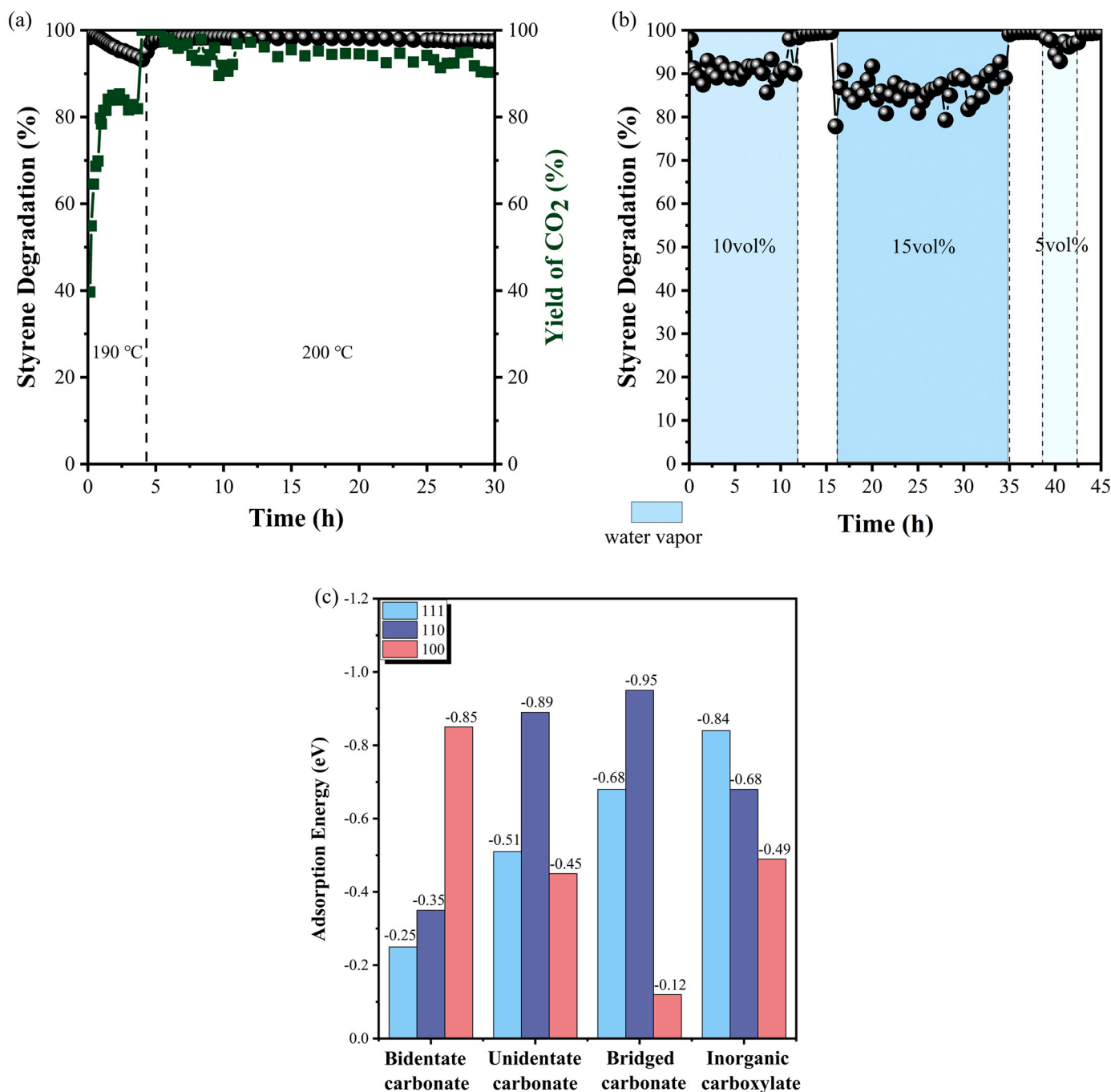


**Fig. 6.** (a) The styrene catalytic oxidation durability test of CeO<sub>2</sub>-C<sub>8</sub>H<sub>8</sub>-130-24 under 400 ppm styrene (190/200 °C), and WHSV = 30,000 mL/(g·h). (b) The styrene catalytic oxidation durability test with water vapor (15/10/5 vol%) of CeO<sub>2</sub>-C<sub>8</sub>H<sub>8</sub>-130-24 under 100 ppm styrene at 200 °C, and WHSV = 30,000 mL/(g·h). (c) The adsorption energy of (111), (110), and (100) crystal faces for bidentate carbonate, unidentate carbonate, bridged carbonate and inorganic carboxylate.

C<sub>8</sub>H<sub>8</sub>-130-24 occurs at 83.3 °C, which is a significantly lower temperature than that of CeO<sub>2</sub>-C<sub>8</sub>H<sub>8</sub>-130-18 (88.1 °C), CeO<sub>2</sub>-C<sub>8</sub>H<sub>8</sub>-130-12 (92.9 °C), and CeO<sub>2</sub>-C<sub>8</sub>H<sub>8</sub>-130-6 (93.8 °C). This shows that strong physically adsorbed styrene can undergo catalytic oxidation reactions with oxygen below 100 °C. These results demonstrate that styrene can be adsorbed and activated more easily on CeO<sub>2</sub>-C<sub>8</sub>H<sub>8</sub>-130-24 than on the other three catalysts.

Styrene-TPSR was also performed under a N<sub>2</sub> atmosphere for CeO<sub>2</sub>-C<sub>8</sub>H<sub>8</sub>-130-24 and CeO<sub>2</sub>-C<sub>8</sub>H<sub>8</sub>-130-12 (Fig. S20(c)-(d)) to study the importance of oxygen molecules in the catalytic oxidation of styrene. Under the O<sub>2</sub> atmosphere, more gas-phase oxygen can be adsorbed and activated at the same time to form reactive oxygen species, meaning that

the lattice oxygen species are replenished more rapidly. This results in a higher level of CO<sub>2</sub> production at 150 °C under the O<sub>2</sub> atmosphere compared to the N<sub>2</sub> atmosphere for both CeO<sub>2</sub>-C<sub>8</sub>H<sub>8</sub>-130-24 and CeO<sub>2</sub>-C<sub>8</sub>H<sub>8</sub>-130-12. Under both atmospheres, the first CO<sub>2</sub> formation peak is similar, indicating that the adsorbed oxygen species react with the surface-adsorbed styrene in an oxidation process. However, the temperature of this CO<sub>2</sub> formation peak is lower under the O<sub>2</sub> atmosphere (83.3 °C /183.3 °C /245 °C) than under the N<sub>2</sub> atmosphere (90.5 °C /196.6 °C /290 °C), demonstrating the important complementary role of oxygen molecules in the catalytic oxidation of styrene. Interestingly, more styrene is involved in the reaction in the O<sub>2</sub> atmosphere. Thus, the intensity of the shoulder peak of CeO<sub>2</sub>-C<sub>8</sub>H<sub>8</sub>-130-12 at 113 °C is smaller



in the O<sub>2</sub> atmosphere (Fig. S20(d)). However, this phenomenon is different for CeO<sub>2</sub>-C<sub>8</sub>H<sub>8</sub>-130–24. Even in the N<sub>2</sub> atmosphere, the abundant lattice oxygen species rapidly migrate to the surface of CeO<sub>2</sub>-C<sub>8</sub>H<sub>8</sub>-130–24 to participate in the reaction, forming CO<sub>2</sub> (Fig. S20(c)), under the O<sub>2</sub> atmosphere, more styrene participates in the subsequent reaction (Fig. S20(c)). This is because the cyclic regeneration of oxygen vacancies occurs more frequently in the O<sub>2</sub> atmosphere. At 125 °C, more styrene is desorbed easily and reacts with oxygen. However, due to insufficient oxygen supply, complete oxidation of the desorbed styrene to CO<sub>2</sub> is not achieved. As the temperature further increases to 183 °C, the chemisorbed styrene that is desorbed can be fully oxidized, resulting in more CO<sub>2</sub> compared to the N<sub>2</sub> atmosphere. It is worth noting that the peak of CO<sub>2</sub> generated under the O<sub>2</sub> atmosphere occurs earlier than the peak of CO<sub>2</sub> generated under the N<sub>2</sub> atmosphere for CeO<sub>2</sub>-C<sub>8</sub>H<sub>8</sub>-130–24. This also indicates that the abundant grain boundaries of CeO<sub>2</sub>-C<sub>8</sub>H<sub>8</sub>-130–24 lead to the formation of oxygen vacancies, thus promoting styrene catalytic oxidation over this catalyst.

### 3.6.2. In-situ visible Raman spectroscopy

Adsorbed oxygen species and the outward migration of lattice oxygen species play an important role in the catalytic oxidation of styrene. Quantitative studies of oxygen vacancy concentrations can indirectly reflect the production and consumption of reactive oxygen species. Therefore, in-situ visible Raman spectroscopy was employed to study the variation of oxygen vacancy concentration during the styrene oxidation reaction. The Raman spectra obtained for the C<sub>8</sub>H<sub>8</sub>-TPSR experiments are shown in Fig. S22. A peak at 461.9 cm<sup>-1</sup> is ascribed to the F<sub>2g</sub> mode of the cubic fluorite CeO<sub>2</sub> phase, and another peak at 598.7 cm<sup>-1</sup> is caused by the defect-induced (D) mode associated with oxygen vacancies [2]. Therefore, the A<sub>D</sub>/A<sub>F2g</sub> ratios of these in-situ Raman spectra were used to describe the change in oxygen vacancy concentration during the C<sub>8</sub>H<sub>8</sub>-TPSR experiment to provide further insight into how oxygen vacancies and carbon-coke formation change as the styrene catalytic oxidation reaction proceeds with increasing temperature.

As shown in Fig. S22 (a)–(b), the A<sub>D</sub>/A<sub>F2g</sub> ratio of CeO<sub>2</sub>-C<sub>8</sub>H<sub>8</sub>-130–24 increases from 0.0201 to 0.1018 during the C<sub>8</sub>H<sub>8</sub>-TPSR test as the temperature increases from 30° to 175°C. As the temperature increases to 200 °C, this value sharply drops to 0.0332. The surface adsorbed oxygen species are consumed without being quickly replaced during the early catalytic oxidation reaction, so the oxygen vacancy concentration increases at low temperatures. As the temperature increases, the lattice oxygen species and surface lattice oxygen species are activated and gradually migrate outward. At the same time, active oxygen species are formed at the oxygen vacancies and participate in the styrene catalytic oxidation reaction. Therefore, the concentration of oxygen vacancies starts to decrease. The oxygen vacancy concentration slightly increases as the temperature increases from 300° to 350°C, which is mainly because active oxygen species are consumed faster than they are formed. As a comparison, the CeO<sub>2</sub>-C<sub>8</sub>H<sub>8</sub>-130–12 sample was also subjected to in-situ Raman analysis during C<sub>8</sub>H<sub>8</sub>-TPSR testing (Fig. S22(c)–(d)). In agreement with the above UV-Raman and PALS experiments, the oxygen vacancy concentration of CeO<sub>2</sub>-C<sub>8</sub>H<sub>8</sub>-130–12 is lower than that of CeO<sub>2</sub>-C<sub>8</sub>H<sub>8</sub>-130–24 at room temperature. The oxygen vacancy concentration of this catalyst increases between 30 and 200 °C, while a decline occurs at temperatures above 200 °C. This falling temperature point is shifted back (at a higher temperature) compared to that of CeO<sub>2</sub>-C<sub>8</sub>H<sub>8</sub>-130–24, suggesting that the outward migration of lattice oxygen and gas-phase oxygen adsorption-activation are weaker for CeO<sub>2</sub>-C<sub>8</sub>H<sub>8</sub>-130–12 than for CeO<sub>2</sub>-C<sub>8</sub>H<sub>8</sub>-130–24. This is consistent with the H<sub>2</sub>-TPR and O<sub>2</sub>-TPD results. As the temperature rises to 300 °C, the oxygen vacancy concentration declines more significantly. This means that more of the (surface) lattice oxygen of CeO<sub>2</sub>-C<sub>8</sub>H<sub>8</sub>-130–12 migrates outward and is activated at oxygen vacancies to participate in the styrene oxidation

reaction at 300 °C. In summary, this demonstrates that the catalytic oxidation of styrene follows the L-H mechanism at low temperatures and MvK mechanism as the temperature rises [13].

According to Fig. S22(e), with increasing temperature, peaks gradually appear and increase in intensity at 1320, 1410, and 1430 cm<sup>-1</sup> due to the deposition of carbon [47]. These in-situ Raman spectra suggest that when the temperature increases to 150 °C, carbon deposition begins to occur on the catalyst surface. This carbon cannot be removed even when the temperature is reduced back to 30 °C without continuous oxygen inflow (Figs. S22(f-1)–(f-3)). To further validate this hypothesis, TPO experiments under in-situ Raman detection were conducted on the CeO<sub>2</sub>-C<sub>8</sub>H<sub>8</sub>-130–12 catalyst after the C<sub>8</sub>H<sub>8</sub>-TPSR tests. The TPO results clearly demonstrate that the carbon deposition on the catalyst surface can be rapidly eliminated with increasing temperature after the introduction of gas-phase oxygen. Until the temperature reaches 250 °C, there is almost no carbon deposition. The catalyst color changes from black to light yellow after exposure to 250 °C in the TPO test. This is the same color state as that of the fresh catalyst (Figs. S22(f-4)). Therefore, the carbon deposits accumulated on the catalyst surface are soft carbon [21], which can be easily eliminated by raising the temperature and introducing oxygen molecules.

### 3.6.3. In-situ DRIFTS

To further understand the adsorption-oxidation process of styrene on the CeO<sub>2</sub>-C<sub>8</sub>H<sub>8</sub>-130–24 catalyst, in-situ DRIFTS analysis was performed. The attributions of specific bands in the in-situ DRIFTS spectra are listed in Table S6. During the in-situ DRIFTS analysis, the CeO<sub>2</sub>-C<sub>8</sub>H<sub>8</sub>-130–24 catalyst was exposed to styrene/air at different temperatures, and the resulting spectra are shown in Fig. 5(c). As soon as gaseous styrene is introduced to the reaction equipment, bands immediately appear at 1445, 1498, 1526 and 1594 cm<sup>-1</sup>. These bands are attributed to the ν(C=C) bonds of typical aromatic rings in the skeleton [13,48]. Meanwhile, the band at 3069 cm<sup>-1</sup> is related to ν(C-H) stretching vibration of the aromatic ring [13,38]. This shows that styrene is mainly adsorbed on the catalyst surface in the low-temperature range of 30–125 °C. The band located at 917 cm<sup>-1</sup> is ascribed to unsaturated carboxylic acids [21,40], indicating that the aromatic ring cleavage of styrene occurs at room temperature. The bands at 2360 and 2340 cm<sup>-1</sup> are attributed to CO<sub>2</sub> species [18,48]. With increasing temperature, the intensity of the peaks corresponding to various intermediates and the final product CO<sub>2</sub> gradually increase in intensity, indicating that these intermediates are gradually accumulated on the catalyst surface before being oxidized into CO<sub>2</sub>. When the temperature reaches 75 °C, peaks associated with the ν(C-O) stretching vibrations of alcohol species appear between 1200 and 1000 cm<sup>-1</sup> (1198, 1152, 1102, 1099 and 1039 cm<sup>-1</sup>) [37,41]. This indicates the formation of benzyl alcohol species. The bands at 1472 and 3742 cm<sup>-1</sup> can be attributed to methylene and hydroxyl, respectively. These bands indicate that the benzyl alcohol species are formed on the surface of the catalyst [49]. With increasing temperature, an increasing amount of intermediate products accumulate on the surface of the catalyst. Above 200 °C, peaks appear at 2843, 2722, 1783, and 1630 cm<sup>-1</sup>. These peaks are attributed to C=O stretching vibration, indicating the formation of aldehydes [50]. The bands located at around 1736 and 1659 cm<sup>-1</sup> (C=O stretching vibration) can be attributed to benzaldehyde species [40,50]. The bands at 1567, 1543, and 1368 cm<sup>-1</sup> are caused by the antisymmetric vibration and symmetric vibration of the carboxylate group (COOH<sup>-</sup>) in benzoate species [51,52]. The asymmetric (1567 cm<sup>-1</sup>) and symmetric (1368 cm<sup>-1</sup>) vibration bands of benzoate species have a Δν of 175 cm<sup>-1</sup>, which is close to the free ion values. This suggests that benzoate ions are adsorbed on the CeO<sub>2</sub>-C<sub>8</sub>H<sub>8</sub>-130–24 surface in the form of a bridge structure. In other words, this proves that carboxylate ions are coordinated with the two oxygen atoms bonded to the same Ce atom [51,53]. The adsorption bands at 3800–3500 cm<sup>-1</sup> are attributed to ν(metal-OH). The maximum

accumulation of intermediate products (benzaldehyde, benzoic acid, etc.) on the catalyst surface is achieved when the temperature increases to 250 °C. As the temperature continues to rise to 350 °C, the conversion rate increases. At this time, the peak intensities of the intermediate products decrease, indicating that the intermediate products are rapidly consumed and more CO<sub>2</sub> and the incomplete oxidation product CO (2086 cm<sup>-1</sup>) are produced [40,54]. Meanwhile, the characteristic peak at 1368 cm<sup>-1</sup> attributed to carboxylate species tends to increase above 250 °C. The different changes of the two bands (1567 cm<sup>-1</sup> and 1368 cm<sup>-1</sup>) indicate that benzoic acid and carboxylate species are important intermediates before and after the cleavage of the aromatic ring. Styrene is more deeply oxidized with the continuous increase in temperature. At 250 °C, the benzoic acid species generated due to the slower reaction rate are accumulated faster than they can be further oxidized in time, resulting in the accumulation of benzoic acid species on the catalyst surface. A higher reaction rate promotes the more rapid conversion of intermediate products into the final products CO<sub>2</sub> and H<sub>2</sub>O. The peak intensity of the intermediate products generated by the catalytic oxidation of styrene decreases at 350 °C. Therefore, the surface-adsorbed styrene undergoes possible desorption and catalytic conversion into other intermediates or products at this temperature. To further explore the role of gas-phase O<sub>2</sub> in the catalytic process, in-situ DRIFTS was performed while stopping and restarting the flow of oxygen over CeO<sub>2</sub>-C<sub>8</sub>H<sub>8</sub>-130-24 at 200 °C, as shown in Fig. S23. When switching from an aerobic environment to an oxygen-free environment, the IR spectra of some intermediate products significantly change. The CO<sub>2</sub> bands gradually decline within 10 min of cutting off the oxygen. The peaks at 3073 and 1528, 1458 cm<sup>-1</sup> are associated with the  $\nu$ (C-H) stretching vibration of the aromatic ring and  $\nu$ (C-C) skeleton vibrations of the aromatic ring. Additionally, the bands at 1152, 1107, and 1026 cm<sup>-1</sup> (C-O bands) attributed to benzyl alcohol species with the structure C<sub>6</sub>H<sub>5</sub>-CH<sub>2</sub>-O are very weak in the absence of oxygen. The aldehyde species bands (2725, 1692 cm<sup>-1</sup>) are also weaker in the absence of O<sub>2</sub>. The same phenomenon occurs with benzoate species, as indicated by the peaks at 1571 and 1376 cm<sup>-1</sup>. When the catalyst is exposed to oxygen again, more carboxylate species are accumulated on the catalyst surface. Therefore, the presence of oxygen leads to the formation of more alkoxides, aldehydes, and carboxylate species, which accelerates the interaction between the CeO<sub>2</sub>-C<sub>8</sub>H<sub>8</sub>-130-24 catalyst and styrene. The higher reaction rate accelerates the formation of more CO<sub>2</sub> species. Meanwhile, styrene interacts with the catalyst more slowly under oxygen-free conditions, and the reaction rate slows down. These results indicate that gas-phase oxygen is activated by surface oxygen vacancies on the catalyst surface to form more reactive oxygen species, which take part in the oxidation of absorbed styrene, and that the gas-phase oxygen enables the timely replenishment of lattice oxygen via oxygen vacancies.

For comparison, in-situ DRIFTS analysis was conducted over CeO<sub>2</sub>-C<sub>8</sub>H<sub>8</sub>-130-12 under different reaction temperatures (30–350 °C). As shown in Fig. 5(d), when the temperature is above 30 °C, the absorption of styrene on CeO<sub>2</sub>-C<sub>8</sub>H<sub>8</sub>-130-12 leads to the appearance of a series of bands. Several peaks (3068, 3028, 1630, 1499, 1449 and 1398 cm<sup>-1</sup>) that appear in the FTIR spectra are assigned to the  $\nu$ (C-H) stretching vibration of the aromatic ring and  $\nu$ (C-C) skeleton vibrations of the aromatic ring. These characteristic bands of styrene gradually disappeared with increasing reaction temperature. The in-situ DRIFTS spectra adsorption peaks of CeO<sub>2</sub>-C<sub>8</sub>H<sub>8</sub>-130-12 are more complex than those of CeO<sub>2</sub>-C<sub>8</sub>H<sub>8</sub>-130-24. This indicates that when the less active CeO<sub>2</sub>-C<sub>8</sub>H<sub>8</sub>-130-12 catalyst is used for catalytic styrene oxidation, the intermediate products accumulated during the reaction process cannot be further oxidized in a timely manner to generate CO<sub>2</sub> and H<sub>2</sub>O due to the slower reaction rate. The asymmetric and symmetric  $\nu$ (C=O) stretching vibration peaks of the corresponding cyclic anhydride (1961, 1919, and 1826 cm<sup>-1</sup>) are significantly enhanced at 175 and 200 °C, but these peaks are weakened above 200 °C. This shows that the catalytic activity of CeO<sub>2</sub>-C<sub>8</sub>H<sub>8</sub>-130-12 significantly increases above 200 °C. Thus, due to

its slower reaction rate, the CeO<sub>2</sub>-C<sub>8</sub>H<sub>8</sub>-130-12 catalyst has a larger energy barrier that must be overcome for the destruction of the generated intermediate maleic anhydride. The higher activation energy and slower reaction rate of CeO<sub>2</sub>-C<sub>8</sub>H<sub>8</sub>-130-12 mean that this catalyst cannot further oxidize the maleic anhydride, and its accumulation on the catalyst surface occupies some of the active sites. Thus, catalytic activity tends to decrease. In addition, unlike CeO<sub>2</sub>-C<sub>8</sub>H<sub>8</sub>-130-24, the band attributed to benzoate species (1567 cm<sup>-1</sup>) is the most intense at 300 °C for CeO<sub>2</sub>-C<sub>8</sub>H<sub>8</sub>-130-12. This peak weakens in intensity at 350 °C, while the peak of carboxylate species (1380 cm<sup>-1</sup>) is enhanced. The intermediate product bands of CeO<sub>2</sub>-C<sub>8</sub>H<sub>8</sub>-130-12 clearly migrate toward higher temperatures, suggesting that the catalytic oxidation of styrene over CeO<sub>2</sub>-C<sub>8</sub>H<sub>8</sub>-130-12 occurs at a slower rate compared with CeO<sub>2</sub>-C<sub>8</sub>H<sub>8</sub>-130-24.

Furthermore, combining the DRIFT spectra of CeO<sub>2</sub>-C<sub>8</sub>H<sub>8</sub>-130-24 and CeO<sub>2</sub>-NoC<sub>8</sub>H<sub>8</sub>-130-24 at different times shows that the intensities of the detected FTIR bands increase with time, as displayed in Fig. S24. For both samples, the benzyl alcohol species (1178, 1160, 1097, 1071, 1026 cm<sup>-1</sup>), benzaldehyde species (2859, 2832, 2712, 1715 cm<sup>-1</sup>), benzoic acid species and carboxylate species (1594, 1574, 1374 cm<sup>-1</sup>), phenol species (1240 cm<sup>-1</sup>), and maleic anhydride species (1962, 1918, 1815 cm<sup>-1</sup>) bands all gradually increase in intensity with increasing time. Fewer intermediates are generated by CeO<sub>2</sub>-C<sub>8</sub>H<sub>8</sub>-130-24 than by CeO<sub>2</sub>-NoC<sub>8</sub>H<sub>8</sub>-130-24, especially benzoic acid (an important intermediate prior to the ring opening of the aromatic ring). This is mainly because CeO<sub>2</sub>-C<sub>8</sub>H<sub>8</sub>-130-24 has a faster reaction rate (deeper oxidation) than CeO<sub>2</sub>-NoC<sub>8</sub>H<sub>8</sub>-130-24, which is ultimately reflected by the relatively weak intermediate peak intensity in the in-situ DRIFTS spectra.

In summary, in-situ DRIFTS analysis demonstrates that the destruction of maleic anhydride is the important rate-determining step in the catalytic oxidation of styrene[13] as well as the important role of gas-phase oxygen in the oxidation of styrene. Moreover, the optimization of different crystallization temperatures and crystallization time of the induced CeO<sub>2</sub> catalysts in this study effectively modulates the morphology and exposed crystal facets of the catalysts (the more dominant (111) is exposed). This further alters the ability of the induced CeO<sub>2</sub> catalysts to adsorb and activate styrene and gas-phase oxygen, and the migration of lattice oxygen is also modified. Ultimately, the reaction rate of styrene oxidation is significantly affected. It is worth noting that the catalytic oxidation of styrene is not altered by the different crystallization treatments of the induced CeO<sub>2</sub> catalysts. This oxidation process generally takes the following pathway: styrene → benzyl alcohol species → benzaldehyde species → benzoic acid species → phenol..... → maleic anhydride → carboxylate species → CO<sub>2</sub> + H<sub>2</sub>O.

### 3.7. Catalyst durability studies

CeO<sub>2</sub>-C<sub>8</sub>H<sub>8</sub>-130-24 exhibits better durability at 200 °C under 100 ppm styrene, with the conversion rate still almost 100% after 10 h (Fig. S25). The CeO<sub>2</sub>-C<sub>8</sub>H<sub>8</sub>-130-24 and CeO<sub>2</sub>-NoC<sub>8</sub>H<sub>8</sub>-130-24 catalysts have significant differences in terms of both activity and durability. This clearly demonstrates that the conversion rate of gaseous styrene can be significantly improved by adding liquid styrene to the catalyst synthesis process.

As shown in Fig. S26, monodentate carbonate, bridge carbonate and bicarbonate species can be observed on the surface of the reacted CeO<sub>2</sub>-C<sub>8</sub>H<sub>8</sub>-130-24 catalyst (150 °C for 10 h). The accumulation of carbonate has two sources. One is the carbonate species formed after the destruction of maleic anhydride during the catalytic oxidation of styrene. The second is the formation of the final product CO<sub>2</sub>, which causes the formation of bridging carbonates due to the generation of oxygen vacancies. Carbonate accumulation on the catalyst surface means that the carbonate reaction rate is lower than its formation rate. Thus, carbonate will occupy the active sites, leading to catalyst deactivation. This phenomenon is consistent with the in-situ Raman analysis. Fig. 6(a) shows the results of a durability test of CeO<sub>2</sub>-C<sub>8</sub>H<sub>8</sub>-130-24 under a high

concentration of styrene (400 ppm). A conversion rate of 93% is still retained after 4 h, the CO<sub>2</sub> yield remains at around 80%, and less CO is generated. This indicated that the catalyst cannot achieve 100% oxidation and mineralization of the styrene at 190 °C. When the temperature is increased to 200 °C, the styrene conversion gradually returns to about 98%, and a sharp increase in CO<sub>2</sub> (CO<sub>2</sub> yield >100%) can be detected within the next 1 h. This suggests that the carbonate species and carbon deposits accumulated on the catalyst surface are further oxidized, leading to the generation of excess CO<sub>2</sub>. This proves that catalytic performance can be restored by increasing the temperature. Even after 30 h of durability test, the CeO<sub>2</sub>-C<sub>8</sub>H<sub>8</sub>-130-24 still maintains its short rod-like structure with nanospheres surrounding it, and more of the (111) crystal face is exposed (Fig. S27). The CeO<sub>2</sub>-C<sub>8</sub>H<sub>8</sub>-130-24 catalyst has excellent durability at 200 °C compared to other catalysts reported in the literature (refer to Table S5), demonstrating its greater application value for further practical industrial applications.

Actual industrial emissions contain water vapor. Therefore, to investigate catalytic durability in a real environment, CeO<sub>2</sub>-C<sub>8</sub>H<sub>8</sub>-130-24 was tested in a water resistance test in the presence of 15/10/5 vol% water vapor. As shown in Fig. 6(b), styrene degradation is maintained at about 90% in the presence of 10 vol% water vapor during a 12 h reaction at 200 °C. The styrene degradation rate immediately returns to almost 100% when the catalyst is no longer exposed to water vapor. Under 15 vol% water vapor, the styrene degradation is reduced to about 86% after 4 h. Similarly, the styrene conversion is immediately restored to 100% after 19 h of the 15 vol% water resistance experiment. Under 5 vol% water vapor, styrene conversion is maintained at about 96%, and the conversion rate is immediately restored when the water vapor is stopped. This phenomenon is attributed to the competitive adsorption of styrene and water vapor. The water vapor content shows a negative linear correlation with styrene degradation. In general, CeO<sub>2</sub>-C<sub>8</sub>H<sub>8</sub>-130-24 exhibits excellent water resistance.

In conclusion, the CeO<sub>2</sub>-C<sub>8</sub>H<sub>8</sub>-130-24 catalyst dominated by exposed (111) crystal planes has excellent durability, while the CeO<sub>2</sub>-C<sub>8</sub>H<sub>8</sub>-130-12 catalyst dominated by exposed (100) crystal planes has worse durability. To further analyze the effect of the adsorption of different types of carbonates on the crystal faces exposed by the different induced CeO<sub>2</sub> catalysts, DFT theoretical calculations were performed, as shown in Fig. 6(c) and Fig. S28. For bidentate carbonates, the (111) plane has the smallest adsorption energy (−0.25 eV), followed by the (110) plane (−0.35 eV) and the (100) plane (−0.85 eV). Thus, the accumulated bidentate carbonate species are not easily adsorbed on the (111) crystal plane. For monodentate carbonate, the order of adsorption energy is: (110) plane (−0.89 eV) > (111) plane (−0.51 eV) > (100) plane (−0.45 eV). This indicates that monodentate carbonate species are not easily adsorbed on the (111) crystal plane. Bridged carbonates represent the structure of CO<sub>2</sub> molecules adsorbed on oxygen vacancies, and the order of adsorption energy is: (110) crystal plane (−0.95 eV) > (111) crystal plane (−0.68 eV) > (100) crystal plane (−0.12 eV). This indicates that the adsorption energy of CO<sub>2</sub> on the (111) crystal face is moderate. In other words, the generated CO<sub>2</sub> is not easily adsorbed on the (111) crystal plane. However, it is more easily adsorbed on the (110) crystal plane. For inorganic carboxylate, which is a carboxylate species generated during the catalytic oxidation of styrene, the (111) crystal face has the largest adsorption energy (−0.84 eV), followed by the (110) crystal plane (−0.68 eV) and the (100) crystal plane (−0.49 eV). Inorganic carboxylate (formate) is an intermediate product, so a larger adsorption energy is more conducive to its further oxidation on the catalyst surface to generate the subsequent final products (CO<sub>2</sub> and H<sub>2</sub>O). Therefore, this analysis emphasizes that different crystal faces have different adsorption energies for carbonate species on the surface of the catalyst, with the (111) crystal plane being unfavorable for the accumulation of monodentate and bidentate carbonates. Meanwhile, the adsorption energy of the (111) crystal plane for CO<sub>2</sub> adsorption on oxygen vacancies is moderate and the (111) crystal plane facilitates the

adsorption of the inorganic carboxylate intermediate produced by the catalytic oxidation of styrene. This makes the subsequent catalytic oxidation of this intermediate more favorable.

#### 4. Conclusions

In this study, the concept of "using the spear of styrene to attack the shield of styrene" was employed to synthesize a series of induced CeO<sub>2</sub> catalysts for the catalytic oxidation of styrene. During the solvothermal crystallization process, liquid styrene induces the structural evolution of CeO<sub>2</sub> nanocrystals from NS to NR (a short rod-like morphology) and modulates the crystal boundary density of the CeO<sub>2</sub> by changing the crystallization time. The presence of crystal boundaries in the CeO<sub>2</sub>-C<sub>8</sub>H<sub>8</sub>-130-24 catalyst plays an important role in the catalytic oxidation of styrene because these grain boundaries facilitate more lattice distortion. Therefore, more oxygen vacancies (a high Ce<sup>3+</sup> ratio) are formed on the catalyst surface, leading to excellent catalytic activity for the oxidation of styrene. In-situ Raman analysis showed the changes in the oxygen vacancies and coke deposition on the induced CeO<sub>2</sub> catalysts. In-situ DRIFTS was used to study the catalytic oxidation of styrene on the surface of the induced CeO<sub>2</sub> catalysts. Furthermore, DFT theoretical calculations were performed to reveal the relationship between the dominant (111) crystal surface of CeO<sub>2</sub>-C<sub>8</sub>H<sub>8</sub>-130-24 and the accumulated carbonate species on its surface. DFT was also used to further investigate the effect of this crystal plane on catalytic performance. In summary, the synthesis, characterization, and properties of the induced CeO<sub>2</sub> catalysts reported herein offer new insight for the future preparation of new catalysts for pollutant oxidation and provide a certain theoretical basis for the practical application of cerium-based catalysts in the catalytic oxidation of styrene.

#### CRediT authorship contribution statement

**Ying Zhang:** Conceptualization, Methodology, Data analysis, Writing – original draft and Editing, Visualization. **Wenjie Zhu:** Resources, Conceptualization, Supervision, Data curation, Writing – reviewing & editing. **Jichang Lu:** Resources, Writing – review & editing, Supervision. **Wei Liao:** Validation, Software. **Ning Qi:** Resources. **Yongming Luo:** Resources, Data curation. **Dionysios D. Dionysiou:** Resources, Writing – review & editing.

#### Declaration of Competing Interest

The authors declare that they have no known competing financial interests or personal relationships that could have appeared to influence the work reported in this paper.

#### Data Availability

Data will be made available on request.

#### Acknowledgements

We gratefully acknowledge the financial supports of the National Natural Science Foundation of China (No. 22166021, 42030712, 22106055), Yunnan Major Scientific and Technological Projects (Grant No. 202302AG050002-1/KKAU202322027), Science and Technology Plan Project of Yunnan Provincial Science and Technology Department (No.202001AT070035 and 202201AT070086), Key Project of Natural Science Foundation of Yunnan Province (No. 202101AS070026), and Yunnan Provincial Key Laboratory of Micro and Nano Materials and Technologies Open Subjects (2020KFJJ01). The authors gratefully acknowledge the assistance provided by Minghu Zhang and Professor Sufang He in improving the experiments and the paper.



## Appendix A. Supporting information

Supplementary data associated with this article can be found in the online version at [doi:10.1016/j.apcatb.2023.123461](https://doi.org/10.1016/j.apcatb.2023.123461).

## References

- [1] C. Xie, D. Yan, H. Li, S. Du, W. Chen, Y. Wang, Y. Zou, R. Chen, S. Wang, Defect chemistry in heterogeneous catalysis: recognition, understanding, and utilization, *ACS Catal.* 10 (2020) 11082–11098.
- [2] X. Lin, S. Li, H. He, Z. Wu, J. Wu, L. Chen, D. Ye, M. Fu, Evolution of oxygen vacancies in  $\text{MnO}_x\text{-CeO}_2$  mixed oxides for soot oxidation, *Appl. Catal. B Environ.* 223 (2018) 91–102.
- [3] J. Lu, J. Zhong, Q. Ren, J. Li, L. Song, S. Mo, M. Zhang, P. Chen, M. Fu, D. Ye, Construction of Cu-Ce interface for boosting toluene oxidation: Study of Cu-Ce interaction and intermediates identified by in situ DRIFTS, *Chin. Chem. Lett.* 32 (2021) 3435–3439.
- [4] Z.F. Bian, T. Tachikawa, P. Zhang, M. Fujitsuka, T. Majima, A nanocomposite superstructure of metal oxides with effective charge transfer interfaces, *Nat. Commun.* 5 (2014) 3038.
- [5] X. Feng, J. Guo, X. Wen, M. Xu, Y. Chu, S. Yuan, Enhancing performance of Co/ $\text{CeO}_2$  catalyst by Sr doping for catalytic combustion of toluene, *Appl. Surf. Sci.* 445 (2018) 145–153.
- [6] R. Peng, S. Li, X. Sun, Q. Ren, L. Chen, M. Fu, J. Wu, D. Ye, Size effect of Pt nanoparticles on the catalytic oxidation of toluene over Pt/ $\text{CeO}_2$  catalysts, *Appl. Catal. B Environ.* 220 (2018) 462–470.
- [7] W. Yu, W. Wang, S. Li, X. Fu, X. Wang, K. Wu, R. Si, C. Ma, C. Jia, C. Yan, Construction of active site in a sintered copper-ceria nanorod catalyst, *J. Am. Chem. Soc.* 141 (2019) 17548–17557.
- [8] M. Liu, X. Wu, S. Liu, Y. Gao, Z. Chen, Y. Ma, R. Ran, D. Weng, Study Ag. / $\text{CeO}_2$  Catal. Naphtha Oxid.: Balanc. Oxyg. Availab. Oxyg. Regen. Capacit. 219 (2017) 231–240.
- [9] J.F. Chen, H. Yi, Self-assembly of flower-like  $\text{CeO}_2$  microspheres via a template-free synthetic approach and its use as support in enhanced CO and benzene oxidation activity, *Adv. Des. Technol. PTS* 1–3 (2011) 656.
- [10] Y. Guo, Y. Gao, X. Li, G. Zhuang, K. Wang, Y. Zheng, D. Sun, J. Huang, Q. Li, Catalytic benzene oxidation by biogenic Pd nanoparticles over 3D-ordered mesoporous  $\text{CeO}_2$ , *Chem. Eng. J.* 362 (2019) 41–52.
- [11] Y. He, X. Liang, B. Chen, Surface selective growth of ceria nanocrystals by CO absorption, *Chem. Commun.* 49 (2013) 9000–9002.
- [12] Y.H. He, X. Liang, B.H. Chen, Globin-like mesoporous  $\text{CeO}_2$ : A CO-assisted synthesis based on carbonate hydroxide precursors and its applications in low temperature CO oxidation, *Nano Res* 8 (2015) 1269–1278.
- [13] Y. Zhang, J. Lu, L. Zhang, T. Fu, J. Zhang, X. Zhu, X. Gao, D. He, Y. Luo, D. Dionysiou, W. Zhu, Investigation into the catalytic roles of oxygen vacancies during gaseous styrene degradation process via  $\text{CeO}_2$  catalysts with four different morphologies, *Appl. Catal. B Environ.* 309 (2022), 121249.
- [14] Y. Zhu, C. Li, C. Liang, S. Li, X. Liu, X. Du, K. Yang, J. Zhao, Q. Yu, Y. Zhai, Y. Ma, Regulating  $\text{CeO}_2$  morphologies on the catalytic oxidation of toluene at lower temperature: a study of the structure–activity relationship, *J. Catal.* 418 (2023) 151–162.
- [15] A. Ismail, M. Zahid, S. Ali, Su.H. Bakhtiar, N. Ali, A. Khan, Y. Zhu, Engineering of oxygen vacancy defect in  $\text{CeO}_2$  through Mn doping for toluene catalytic oxidation at low temperature, *Environ. Res.* 226 (2023), 115680.
- [16] Y. Zheng, Y. Su, C. Pang, L. Yang, C. Song, N. Ji, D. Ma, X. Lu, R. Han, Q. Liu, Interface-enhanced oxygen vacancies of cocuox catalysts in situ grown on monolithic cu foam for voc catalytic oxidation, *Environ. Sci. Technol.* 56 (2022) 1905–1916.
- [17] X. Wei, K. Li, X. Zhang, Q. Tong, J. Ji, Y. Cai, B. Gao, W. Zou, L. Dong,  $\text{CeO}_2$  nanosheets with anion-induced oxygen vacancies for promoting photocatalytic toluene mineralization: toluene adsorption and reactive oxygen species, *Appl. Catal. B Environ.* 317 (2022), 121694.
- [18] S. Jiang, C. Li, Y. Muhammad, Y. Tang, R. Wang, J. Li, J. Li, Z. Zhao, Z. Zhao, Solvent-induced fabrication of Cu/ $\text{MnO}_x$  nanosheets with abundant oxygen vacancies for efficient and long-lasting photothermal catalytic degradation of humid toluene vapor, *Appl. Catal. B Environ.* 328 (2023), 122509.
- [19] Q.Y. Lian, L.L. Hu, D.R. Ma, Y.M. Jiao, D.H. Xia, Y.J. Huang, Z.Y. Tang, W. Qu, H. N. Zhao, C. He, D.D. Gang, Interstitial atomic Bi charge-alternating processor boosts twofold molecular oxygen activation enabling rapid catalytic oxidation reactions at room temperature, *Adv. Funct. Mater.* 32 (2022), 2205054.
- [20] Z. Su, X. Li, W. Si, L. Artiglia, Y. Peng, J. Chen, H. Wang, D. Chen, J. Li, Probing the actual role and activity of oxygen vacancies in toluene catalytic oxidation: evidence from in situ XPS/NEXAFS and DFT + U calculation, *ACS Catal.* (2023) 3444–3455.
- [21] Y. Zhang, L.M. Zhang, J.C. Lu, W. Liao, J. Zhang, X.Y. Gao, Y.M. Luo, W.J. Zhu, Investigation of defect-rich  $\text{CeO}_2$  catalysts for super low-temperature catalytic oxidation and durable styrene removal, *Chemosphere* 303 (2022), 134863.
- [22] K. Wang, C. Zhao, N. Wei, J. Yun, X. Hu, X. Jiang, R. Chu, Z. Tong, Y. Zou, Z. Chen, Insight into low-temperature styrene oxidation over nano  $\text{CeO}_2$  catalysts: modulating Ce–O bond strength to construct oxygen defect engineering, *ACS EST Eng* 3 (2023) 1098–1111.
- [23] Z. Jiang, M. Jing, X. Feng, J. Xiong, C. He, M. Douthwaite, L. Zheng, W. Song, J. Liu, Z. Qu, Stabilizing platinum atoms on  $\text{CeO}_2$  oxygen vacancies by metal-support interaction induced interface distortion: mechanism and application, *Appl. Catal. B Environ.* 278 (2020), 119304.
- [24] J.Q. Wang, C. Xi, M. Wang, L. Shang, J. Mao, C.-K. Dong, H. Liu, S.A. Kulinich, X. W. Du, Laser-generated grain boundaries in ruthenium nanoparticles for boosting oxygen evolution reaction, *ACS Catal.* 10 (2020) 12575–12581.
- [25] Z. Zhang, I. Karimata, H. Nagashima, S. Muto, K. Ohara, K. Sugimoto, T. Tachikawa, Interfacial oxygen vacancies yielding long-lived holes in hematite mesocrystal-based photoanodes, *Nat. Commun.* 10 (2019) 4832.
- [26] Z.A. Su, W.Z. Si, H. Liu, S.C. Xiong, X.F. Chu, W.H. Yang, Y. Peng, J.J. Chen, X. Z. Cao, J.H. Li, Boosting the Catalytic Performance of  $\text{CeO}_2$  in Toluene Combustion via the Ce–Ce Homogeneous Interface, *Environ. Sci. Technol.* 55 (2021) 12630–12639.
- [27] Q. Quan, H. Wen, S. Han, Z. Wang, Z. Shao, M. Chen, Fluorous-Core nanoparticle-embedded hydrogel synthesized via tandem photo-controlled radical polymerization: facilitating the separation of perfluorinated alkyl substances from water, *ACS Appl. Mater. Interfaces* 12 (2020) 24319–24327.
- [28] H. Gong, Y. Gu, Y. Zhao, Q. Quan, S. Han, M. Chen, Precise synthesis of ultra-high-molecular-weight fluoropolymers enabled by chain-transfer-agent differentiation under visible-light irradiation, *Angew. Chem. Int. Ed.* 59 (2020) 919–927.
- [29] P.F. Wang, X.L. Ma, X.G. Hao, B. Tang, A. Abudula, G.Q. Guan, Oxygen vacancy defect engineering to promote catalytic activity toward the oxidation of VOCs: a critical review, *Catal. Rev. Sci. Eng.* (2022), 2078555.
- [30] H.A. Rangkooy, M.N. Pour, B.F. Dehaghi, Efficiency evaluation of the photocatalytic degradation of zinc oxide nanoparticles immobilized on modified zeolites in the removal of styrene vapor from air, *Korean J. Chem. Eng.* 34 (2017) 3142–3149.
- [31] J.Y. Shi, J.Y. Chen, G.Y. Li, T.C. An, H. Yamashita, Fabrication of Au/ $\text{TiO}_2$  nanowires@carbon fiber paper ternary composite for visible-light photocatalytic degradation of gaseous styrene, *Catal. Today* 281 (2017) 621–629.
- [32] J.Y. Chen, Z.G. He, Y.M. Ji, G.Y. Li, T.C. An, W.Y. Choi,  $\cdot\text{OH}$  radicals determined photocatalytic degradation mechanisms of gaseous styrene in  $\text{TiO}_2$  system under 254 nm versus 185 nm irradiation: Combined experimental and theoretical studies, *Appl. Catal. B Environ.* 257 (2019), 117912.
- [33] J. Wu, J. Wang, C. Liu, C. Nie, T. Wang, X. Xie, J. Cao, J. Zhou, H. Huang, D. Li, S. Wang, Z. Ao, Removal of gaseous volatile organic compounds by a multiwalled carbon nanotubes/peroxymonosulfate wet scrubber, *Environ. Sci. Technol.* 56 (2022) 13996–14007.
- [34] Y. Yang, Y. Qian, Z. Luo, H. Li, L. Chen, X. Cao, S. Wei, B. Zhou, Z. Zhang, S. Chen, W. Yan, J. Dong, L. Song, W. Zhang, R. Feng, J. Zhou, K. Du, X. Li, X.-M. Zhang, X. Fan, Water induced ultrathin  $\text{Mo}_2\text{C}$  nanosheets with high-density grain boundaries for enhanced hydrogen evolution, *Nat. Commun.* 13 (2022) 7225.
- [35] G. Xiao, S. Xin, H. Wang, R.J. Zhang, Q. Wei, Y.X. Lin, Catalytic oxidation of styrene over ce-substituted  $\text{La}_{1-x}\text{Ce}_x\text{MnO}_3$  catalysts, *Ind. Eng. Chem. Res.* 58 (2019) 5388–5396.
- [36] Z. Su, W. Yang, C. Wang, S. Xiong, X. Cao, Y. Peng, W. Si, Y. Weng, M. Xue, J. Li, Roles of oxygen vacancies in the bulk and surface of  $\text{CeO}_2$  for toluene catalytic combustion, *Environ. Sci. Technol.* 54 (2020) 12684–12692.
- [37] K. Zhang, L. Dai, Y. Liu, J. Deng, L. Jing, K. Zhang, Z. Hou, X. Zhang, J. Wang, Y. Feng, Y. Zhang, H. Dai, Insights into the active sites of chlorine-resistant Pt-based bimetallic catalysts for benzene oxidation, *Appl. Catal. B Environ.* 279 (2020), 119372.
- [38] X. Wan, L. Wang, S. Gao, X. Lang, L. Wang, T. Zhang, A. Dong, W. Wang, Low-temperature removal of aromatics pollutants via surface labile oxygen over Mn-based mullite catalyst  $\text{SmMn}_2\text{O}_5$ , *Chem. Eng. J.* 410 (2021), 128305.
- [39] J. Fan, Y. Sun, M. Fu, J. Li, D. Ye, Modulate the metal support interactions to optimize the surface-interface features of Pt/ $\text{CeO}_2$  catalysts for enhancing the toluene oxidation, *J. Hazard. Mater.* 424 (2022), 127505.
- [40] W. Yang, Z. Su, Z. Xu, W. Yang and Y. Peng, J. Li, Comparative study of  $\alpha$ -,  $\beta$ -,  $\gamma$ - and  $\delta$ - $\text{MnO}_2$  on toluene oxidation: Oxygen vacancies and reaction intermediates, *Appl. Catal. B Environ.* 260 (2019) 118150.
- [41] J. Zhong, Y. Zeng, D. Chen, S. Mo, M. Zhang, M. Fu, J. Wu, Z. Su, P. Chen, D. Ye, Toluene oxidation over  $\text{Co}^{3+}$ -rich spinel  $\text{Co}_3\text{O}_4$ : Evaluation of chemical and by-product species identified by in situ DRIFTS combined with PTR-TOF-MS, *J. Hazard. Mater.* 386 (2020), 121957.
- [42] X. Chen, X. Chen, E. Yu, S. Cai, H. Jia, J. Chen, P. Liang, In situ pyrolysis of Ce-MOF to prepare  $\text{CeO}_2$  catalyst with obviously improved catalytic performance for toluene combustion, *Chem. Eng. J.* 344 (2018) 469–479.
- [43] Q. Yu, C. Li, J. Zhao, X. Liu, L. Huang, Y. Zhu, K. Yang, Z. Zhang, D. Ma, Y. Zhang, Q. Huang, Efficient photothermal catalytic oxidation of toluene by  $\text{La}_{1-x}\text{Fe}_x\text{MnO}_3$  with full spectrum response: The effects of Fe doping and photoactivation, *Appl. Catal. B Environ.* 327 (2023), 122441.
- [44] J. Kong, Z. Xiang, G. Li, T. An, Introduce oxygen vacancies into  $\text{CeO}_2$  catalyst for enhanced coke resistance during photothermocatalytic oxidation of typical VOCs, *Appl. Catal. B Environ.* 269 (2020), 118755.
- [45] F. Amano, T. Tanaka, T. Funabiki, Auto-reduction of Cu(II) species supported on  $\text{Al}_2\text{O}_3$  to Cu(I) by thermovacuum treatment, *J. Mol. Catal. A: Chem.* 221 (2004) 89–95.
- [46] J. Fonseca, N. Bion, Y.E. Licea, C.M. Morais, Md.C. Rangel, D. Duprez, F. Epron, Unexpected redox behaviour of large surface alumina containing highly dispersed ceria nanoclusters, *Nanoscale* 11 (2019) 1273–1285.



- [47] C. Li, Y. Sakata, T. Arai, K. Domen, K. Maruya, T. Onishi, Adsorption of carbon monoxide and carbon dioxide on cerium oxide studied by Fourier-transform infrared spectroscopy. Part 2.—Formation of formate species on partially reduced CeO<sub>2</sub> at room temperature, *J. Chem. Soc., Faraday Trans. 1* (85) (1989) 1451–1461.
- [48] S. Mo, Q. Zhang, J. Li, Y. Sun, Q. Ren, S. Zou, Q. Zhang, J. Lu, M. Fu, D. Mo, J. Wu, H. Huang, D. Ye, Highly efficient mesoporous MnO<sub>2</sub> catalysts for the total toluene oxidation: oxygen-vacancy defect engineering and involved intermediates using in situ DRIFTS, *Appl. Catal. B Environ.* 264 (2020), 118464.
- [49] Z. Hou, L. Dai, Y. Liu, J. Deng, L. Jing, W. Pei, R. Gao, Y. Feng, H. Dai, Highly efficient and enhanced sulfur resistance supported bimetallic single-atom palladium-cobalt catalysts for benzene oxidation, *Appl. Catal. B Environ.* 285 (2021), 119844.
- [50] J. Huang, R. Fang, Y. Sun, J. Li, F. Dong, Efficient  $\alpha$ -MnO<sub>2</sub> with (210) facet exposed for catalytic oxidation of toluene at low temperature: a combined in-situ DRIFTS and theoretical investigation, *Chemosphere* 263 (2021), 128103.
- [51] H. Sun, Z. Liu, S. Chen, X. Quan, The role of lattice oxygen on the activity and selectivity of the OMS-2 catalyst for the total oxidation of toluene, *Chem. Eng. J.* 270 (2015) 58–65.
- [52] C. Zhang, C. Wang, H. Huang, K. Zeng, Z. Wang, H. Jia, X. Li, Insights into the size and structural effects of zeolitic supports on gaseous toluene oxidation over MnO<sub>x</sub>/HZSM-5 catalysts, *Appl. Surf. Sci.* 486 (2019) 108–120.
- [53] E. Finocchio, T. Montanari, C. Resini, G. Busca, Spectroscopic characterization of cobalt-containing solid catalysts, *J. Mol. Catal. A: Chem.* 204–205 (2003) 535–544.
- [54] K. Li, K. Liu, H. Ni, B. Guan, R. Zhan, Z. Huang, H. Lin, Electric field promoted ultra-lean methane oxidation over Pd-Ce-Zr catalysts at low temperature, *Mol. Catal.* 459 (2018) 78–88.